LAWRENCE
LIVERMORE
NATIONAL
LABORATORY

LLNL-JRNL-707920

Large-eddy simulation of shallow cumulus over land: A composite case based on ARM long-term observations at its Southern Great Plains site

Y. Zhang, S. A. Klein, S. Xie, S. Tang, J. Fan, A. S. Chandra, P. Kollias

November 2, 2016

Journal of Atmospheric Sciences

Disclaimer

Large-eddy simulation of shallow cumulus over land: A composite case based on ARM long-term observations at its Southern Great Plains site

Yunyan Zhang* and Stephen A. Klein

Lawrence Livermore National Laboratory, Livermore, California

Jiwen Fan

Pacific Northwest National Laboratory, Richland, Washington

Arunchandra S. Chandra

Division of Meteorology and Physical Oceanography, University of Miami, Miami, Florida

Pavlos Kollias

School of Marine and Atmospheric Sciences, Stony Brook University, New York

Shaocheng Xie and Shuaiqi Tang

Lawrence Livermore National Laboratory, Livermore, California

Corresponding author address: Yunyan Zhang, Atmospheric, Earth & Energy Division, Lawrence Livermore National Laboratory, Mail Code L-103, P.O. Box 808, Livermore, CA 94551

E-mail: zhang25@llnl.gov

ABSTRACT

Based on long-term observations by the Atmospheric Radiation Measurement program at its Southern Great Plains site, a new composite case of continental shallow cumulus (ShCu) convection is constructed for large-eddy simulations (LES) and single-column models. The case represents a typical daytime non-precipitating ShCu whose formation and dissipation are driven by the local atmospheric conditions and land-surface forcing, and are not influenced by synoptic weather events. The case includes: early-morning initial profiles of temperature and moisture with a residual layer; diurnally-varying sensible and latent heat fluxes which represent a domain average over different land-surface types; simplified large-scale horizontal advective tendencies and subsidence; and horizontal winds with prevailing direction and average speed. Observed composite cloud statistics are provided for model evaluation.

The observed diurnal cycle is well-reproduced by LES, however the cloud amount, liquid water path, and shortwave radiative effect are generally underestimated. LES are compared between simulations with an all-or-nothing bulk microphysics and a spectral bin microphysics. The latter shows improved agreement with observations in the total cloud cover and the amount of clouds with depths greater than 300 meters. When compared with radar retrievals of in-cloud air motion, LES produce comparable downdraft vertical velocities, but a larger updraft area, velocity and updraft mass flux. Both observation and LES show a significantly larger in-cloud downdraft fraction and downdraft mass flux than marine ShCu.

1. Introduction

Correctly simulating the diurnal cycle of convection over land has always been a challenge for conventional global climate models (GCMs) and other large-scale models such as those used for numerical weather prediction. The incorrect diurnal variation of clouds and precipitation is often attributed to the lack of a gradual development of shallow cumulus (ShCu) clouds (**?**). As ShCu's intrinsic horizontal scale is around 1 km or less, conventional GCMs which have horizontal resolutions of 10 to 100 km or greater must parameterize the physical processes associated with ShCu. During GCMs' development and improvement, it has become routine to test new parameterizations through a single-column model simulation of well-developed observationally-based "golden day" large-eddy simulation (LES) cases. These golden day cases are supposed to be representative of stereotypical convection regimes. For almost two decades, the Atmospheric Radiation Measurement (ARM) Southern Great Plains (SGP) non-stationary shallow cumulus case on June 21, 1997 (hereafter ARM97) has been widely used as one of these golden days and as a benchmark for continental shallow convection (**??**). Almost every newly developed convection scheme related to shallow cumulus has been tested using the ARM97 case (**??????????????**). But with such a heavily reliance on this one "golden day" case, one must ask: does it really represent the classic convective ShCu regime as we expect it to be? (**?**)

Figure 1a-b shows that on the day used for ARM97, the primary cloud fraction peak was around 0800 local standard time (LST) and large-scale cloud systems were approaching SGP from north around 1100 LST. Although the clouds did show a secondary peak in early afternoon with cloud base rising from morning to afternoon, the ARM97 case may not be a good representation of purely local surface-forced continental shallow convection as the ShCu development later in the day was subject to large-scale influence and the morning peak of cloud fraction also hints at a disturbance

in early-morning initial conditions. Indeed, the initial sounding used in ARM97 was substantially modified from the observed sounding (**?**). Thus the ARM97 case does not represent a day free of synoptic influence nor is it conceptually simple enough to permit improved understanding of cloud processes for the purpose of convectional parameterizations.

Therefore it would be desirable to have a new case for shallow convection over land. One possibility is the 3-day case study from a recent ARM field campaign that utilizes the updated ARM instrumentation supplemented by aircraft (RACORO, **????**). However, in addition to the "golden day" approach, we think it worthwhile to develop a new composite case that takes advantage of the long-term continuous ground-based observational data, such as has been collected at ARM (**?**) or European sites (**??**). In particular, we wish to use a case library of locally-generated surface-forced ShCu that has been established based on summertime observations of 13 yr at the ARM SGP site (**???**). Figure 1c shows the satellite image for one of the days in our case library and Figure 1d shows the cloud fraction vertical profile for the composite mean of this case library. From these figures, it is apparent that the ARM97 case does not have the typical diurnal evolution of ShCu. In this study, a new composite case called Continental Active Surface-forced Shallow cumulus (CASS), is built upon these long-term observations for LES and single-column models.

There are three benefits of building a composite modeling case with a strong link to observations. First, it allows us to use the advanced ARM cloud retrieval data that have been developed since 1997. These retrievals provide valuable information about the cloud size distribution, cloud vertical extent, cloud vertical velocity and mass fluxes. Such availability of observational data was almost completely lacking for the ARM97 case.

Second, a composite case allows us to create reliable statistics for the observations that come from vertically pointing instruments such as cloud radar, lidar, and ceilometer. This is a particularly acute issue for shallow cumulus due to the intermittent nature and limited sample of clouds

on an individual day (**??**). For instance, with the vertically pointing millimeter wavelength cloud radar at the ARM SGP site, and a usual ShCu cloud fraction of 30% at the diurnal maximum, there are only about 100 10-second cloudy profiles per hour on a single day. Furthermore, with an average cloud size of 1 km (**?**) and wind speed of 7 m s^{-1}, there might be less than 10 individual clouds observed in an hour. This results in noisy data and large uncertainties for cloud statistics on an individual day. With a composite case, the uncertainty due to sample size will be greatly reduced by the accumulation of these statistics over many days with ShCu. The reduction of such uncertainty is very important to generate reliable observations of cloud statistics for model validation.

Third, by constructing a composite case (consisting of multiple "golden days"), one can identify the dominant environmental forcing of shallow cumulus. No matter how carefully we select our cases, a single-day observation, especially by instruments mostly vertically staring at point locations, is subject to random noises due to synoptic or shorter temporal variabilities or spatial heterogeneities. From the perspective of model input, compositing helps reduce uncertainties in initial and boundary conditions and large-scale advective tendencies and is superior to a single golden day case in representing the most typical conditions of atmospheric and surface environmental factors driving ShCu development.

The composite case represents the evolution of ShCu responding to the average diurnal-varying forcing based on an ensemble of individual ShCu days. Indeed we view this composite case as a viable addition to the ensemble approach in which LES is integrated for every day in our case library. We find that the composite case well represents the mean behavior of the ensemble of LES runs although there is spread due to day-to-day variability (see Appendix). This demonstrates the ability of the composite case to represent the average behavior of many shallow cumulus days and

endorses the aforementioned benefits. In addition, ensemble runs of many ShCu days require large computational resources; the composite approach is economic and relatively easy to be realized.

In this paper, we describe the construction of the new composite case CASS, the results of LES performed for CASS, and the comparison to ARM observations including cloud-scale vertical velocity and mass flux. Specifically, details of the LES model and observation data are presented in section 2; the CASS composite case is described in section 3; the comparison of LES to general ARM observations is shown in section 4; the comparison with observed vertical velocity data is shown in section 5; and conclusions are drawn in section 6.

2. Model description and observational data

a. System for Atmospheric Modeling (SAM)

The System for Atmospheric Modeling (SAM, **?**) is widely used in cloud studies. SAM has a non-hydrostatic anelastic dynamical core and is configured for large-eddy simulation with periodic boundary conditions. In this study, sub-grid scale mixing is represented with a 1.5-order turbulence closure based on a prognostic equation for the sub-grid scale turbulent kinetic energy. Advection of all scalar prognostic variables is done using a monotonic and positive-definite advection scheme in flux form. A Newtonian damping layer is implemented in the upper third of the domain to reduce gravity wave reflection and buildup. Longwave and shortwave radiation are calculated using the Rapid Radiative Transfer Model (RRTMG, **??**). Two cloud and precipitation microphysical packages are used: one is the default one-moment diagnostic bulk microphysics of precipitation and cloud water (**?**); the other is a size-resolved spectrum bin microphysics (**??**). With the bin microphysics, cloud droplet concentration is prognostic, and droplet nucleation is calculated from the predicted supersaturation and specified aerosol size distribution according to the

Köhler theory. Aerosol number concentration is set to 600 cm^{-3} representing a typical continental clean aerosol condition such as SGP (**?**).

Our simulations start at 0530 LST and end at 1730 LST and have a domain 28.8 km by 28.8 km in the horizontal and 16 km in vertical. Horizontal resolution is 50 m and vertical resolution is 20 meters under 5 km with a stretched grid above. This resolution is similar to the cloud radar observed volume. Radar retrievals are provided for each vertical range gate of 45 m, and with a wind speed around 7 m s^{-1}, the horizontal distance sampled by the radar is about 70 m for each 10-second retrieval.

SAM is run with a 1-second time step with RRTMG being called every minute. For the calculation of solar radiation, the day is set up to be July 24th (the 205th day in a year) at the central facility of the ARM SGP site, 36.5^0 N, 97.5^0 W. This represents the average solar insolation of the active shallow cumulus days from May to August in our case library. For radiation calculations above 16 km, the vertical profiles of radiatively important trace gases, water vapor, CO_2, O_3 and temperature are assumed to be those of a mid-latitude summertime climatology. The LES is forced with the large-scale horizontal advective tendencies for temperature and water vapor and a subsidence rate derived from long-term continuous forcing data. Temperature and humidity above 5 km are nudged towards the composite profile for the purpose of radiation calculations with a nudging time-scale of 1 hour. Horizontal winds are nudged towards the composite winds derived from the continuous forcing with a nudging time-scale of 1 hour. The surface roughness length was set to 0.035 m, a characteristic value for the ARM SGP site suggested by ARM97. Turbulence was initiated by imposing random temperature perturbations at each grid point in the lowest 200 m with a maximum amplitude at any model level decreasing linearly from 0.1 K at the surface to zero at 200 m following ARM97. The surface fluxes are specified from observations as discussed later.

b. ARM data

The major observational data streams used in this study are all from the ARM data archives:

- Active Remotely-Sensed Cloud Locations (ARSCL, http://www.arm.gov/data/vaps/arscl, DOI: 10.5439/1027282) 10-second data for calculations of cloud boundaries, cloud chord length (overpass time multiplied by the wind speed at the cloud base height), total surface-projected cloud fraction, and an area fraction covered by clouds whose vertical extent is greater than 300 meters (hereafter "cloud fraction 300m+"). ARSCL is derived from observations of the cloud radar, micropulse lidar and laser ceilometer (**?**).

- Continuous forcing (http://www.arm.gov/data/eval/29, DOI: 10.5439/1273323) for large-scale advective tendencies and subsidence rate (**??**).

- Microwave radiometer-scaled radio sondes (LSSONDE, http://www.arm.gov/data/vaps/lssonde, DOI: 10.5439/1027294) for the vertical profiles of temperature, humidity and horizontal winds.

- Best-estimate fluxes of sensible and latent heat from Energy Balance Bowen Ratio (EBBR) stations (BAEBBR, http://www.arm.gov/data/vaps/baebbr, DOI: 10.5439/1027268) and Quality Controlled Eddy Correlation Flux Measurements (QCECOR, http://www.arm.gov/data/vaps/qcecor, DOI: 10.5439/1097546) over different land types, such as grassland and cropland.

- Column-integrated liquid water path (LWP) from MicroWave Radiometer Retrievals (MWRRET, http://www.arm.gov/data/vaps/mwrret, DOI: 10.5439/1027369; **?**).

- Horizontal winds from the 915-MHz Radar Wind Profiler (RWP, http://www.arm.gov/data/datastreams/915rwpwindcon, DOI: 10.5439/1025135)

- Surface radiative fluxes (QCRAD, https://www.arm.gov/capabilities/vaps/qcrad, DOI:10.5439/1227214; **?**)

For details on these observations and the calculation of cloud statistics, please refer to the data section in **??**.

Separately observations of cloud-scale vertical velocity, updraft and downdraft fractions and mass fluxes are derived from the multi-year retrieval of in-cloud vertical air motion developed by **?** using observed 10-second profiles from the vertically pointing MilliMeter wavelength Cloud Radar (MMCR). Retrievals assume that the terminal velocity of cloud droplets is considerably smaller than the vertical air motion, such that the observed Doppler velocity of cloud droplets is representative of vertical air motion. This assumption holds well for fair-weather non-precipitating shallow cumulus. Prior to the estimation of the in-cloud mass flux, MMCR insect echoes are removed using a fuzzy logic algorithm that uses member functions based on liquid water path, cloud physical thickness, radar reflectivity and spectrum width (**?**). The retrieved vertical velocity data are available since 1997 and overlap well with our case library of observed active shallow cumulus days. At each hour when data is available, we vertically align the 10-second profiles to the hourly-averaged cloud base, and compute the average vertical velocity, area fraction, and mass flux (equal to the product of velocity and area fraction), separately for updrafts and downdrafts. More details on the use of this data in comparison with LES is given in Section 5.

c. Active shallow cumulus days

The new shallow cumulus case is based on the composite of days observed to have ”thick” (or active) shallow cumulus at SGP (refer to Fig.1 in **?**). During May to August in the years 1997 to 2009, we identify 76 thick shallow cumulus days according to selection criteria described in **?**. On these days, shallow cumulus clouds develop locally at SGP and show a strong diurnal cycle

closely tied to surface flux forcing and boundary layer processes. Starting with clear-skies at sunrise, clouds usually appear in the late morning, peak in early afternoon and dissipate before sunset. On each day, there is usually at least 3 hours of clouds observed by radar to compute cloud statistics. Cloud tops are under 4 km and cloud bases gradually rise with time over the day. A rising cloud base is consistent with an entraining boundary layer driven by surface fluxes, as entrainment gradually lowers the value of RH at the surface and thus increases the lifting condensation level (LCL) of surface air (**?**). Note that the observed cloud base is strongly correlated with the calculated LCL from the surface measurements (Fig.14 in **?**). These criteria assure that clouds develop locally and are tied to boundary layer processes.

On active ShCu days, some clouds reach the level of free convection, however further vertical cloud development is limited by low tropospheric relative humidity or an inversion further aloft (**??**). The daily average of active shallow cumulus cloud's vertical extent and horizontal chord length is about 0.7 and 1.0 km respectively. The first cloud onset time varies day to day, ranging from 0800 LST to 1400 LST with an average around 1045 LST. Satellite images are used to confirm that clouds usually develop rather homogeneously in a vast area around SGP and that there is no obvious influence of large-scale weather systems and other cloud types (deep convective hot-tower clouds, cloud anvils or stratiform clouds) in the vicinity of SGP. Although cloud base height differs from day to day, the general progression of cloud development is very similar across the days. It is such simplicity of this observed diurnal behavior that makes these clouds an attractive simulation target for LES or single-column models, and allows us understand their cloud-controlling factors.

3. The CASS composite case

The composite case input data consists of initial profiles, surface boundary conditions and large-scale advective tendencies. All of these quantities are based upon the arithmetic mean of their values on each individual day in our case library with surface-forced active shallow convection.

a. Early morning initial condition

We use sounding data at 0530 LST to composite an initial temperature and humidity profile. Figure 2 shows the original sounding composite which has a smooth transition from the surface stable layer to lower free troposphere boundary layer. However, inspection of individual sounding profiles seldom exhibits such smooth behavior. Instead, almost everyday there is a residual layer or several piece-wise mixed layers between the top of the surface stable layer and an inversion which is around 3 to 3.5 km above ground. The residual layer results from the well-mixed boundary layer of the preceding afternoon before the identified active ShCu day. During nighttime, when the surface cools, the stable boundary layer grows but often only erodes the lower part of this mixed layer. From careful inspection of individual soundings we find that the average depth of stable layer is around 400 meters, while the top of the residual layer is about 1 km. With these characteristics, we reconstruct a residual layer for potential temperature and water vapor mixing ratio conserving specific heat and water vapor in order to avoid extra work for surface-forced daytime boundary layer development. With a residual layer, LES show an onset time that is one hour earlier (not shown); cloud onset time is particularly sensitive to the residual layer in the temperature profile but less sensitive to that in the moisture profile. This is consistent with previous studies showing that the existence of a residual layer enhances boundary-layer-top entrainment due to the lack of temperature stratification in such a layer; as a result, clouds appear earlier (**??**).

Compared with ARM97, our initial sounding is cooler and drier; specifically, it is 2 K colder and 2.5 g kg^{-1} drier in the average below 1 km. In the prescribed initial θ profile of ARM97, the potential temperature vertical gradient ($d\theta/dz$) in the lowest 400 meters, in the lowest 1 km and the layer between 1 and 3 km are 10 K km^{-1}, 6.5 K km^{-1}, and 7 K km^{-1} respectively; while the lapse rates for the same layers in our case are 20 K km^{-1}, 8.5 K km^{-1}, and 4.5 K km^{-1} respectively. The lapse rate in the lower free troposphere is a particular critical parameter affecting the growth of the boundary layer and shallow cumulus development (**?**).

b. Domain mean surface fluxes

The SGP site consists of grassland, cropland and forests. Surface fluxes are separately measured by the older Energy Balance Bowen Ratio (EBBR) Stations, which are typically over grassland, and the newer Eddy Correlation (ECOR) Flux Measurement Systems which are typically over cropland. EBBR data are available at 15 stations for all years covered by our case library. EBBR surface fluxes are constrained by the energy budget based on concurrent radiation and soil heat flux measurements. In contrast, ECOR data are available at 9 stations only since 2004 and thus many of the days in our case library do not have ECOR data. Furthermore, energy budget closure with ECOR data was not achieved until the recent installment of the Surface Energy Balance System (SEBS) in late 2010. Because EBBR and ECOR typically sample different land surface types, it is essential to consider both ECOR and EBBR data to derive domain mean surface fluxes. We construct new surface fluxes shown in Figure 3, in which the total surface flux (sum of latent and sensible heat) is taken from the EBBR composite because of EBBR's longer and more robust energy constraint. The new evaporative fraction (EF, defined as the fraction of surface flux in the form of latent heat) is based on an averaged EF with different weights according to the number of stations from both EBBR and ECOR data. Relative to simulations using only EBBR fluxes,

these new surface fluxes lead to improved agreement with observations for the LES cloud base (see Section A.2).

Compared with ARM97, the daily maximum of the total surface fluxes is 540 W m^{-2} at noon in our case, while the maximum of ARM97 is 650 W m^{-2}. In our case, the latent heat flux peaks at 1300 LST, an hour later than the sensible heat flux; this also happens in ARM97. However, a major difference is that the evaporative fraction of ARM97 is about 0.77, while the EF of our composite case is around 0.63, with a lower value of 0.59 in the morning and a higher value of 0.67 in the afternoon. Across all active shallow cumulus days in our case library, the observed daytime-averaged EF ranges from 0.31 to 0.83 based on the combined EBBR and ECOR data.

c. Large-scale forcing

The composite forcing for our case is calculated from the ARM variational analysis with energy and water budget constraints from both the surface and the top of atmosphere (**??**). While the continuous forcing from variational analysis was generated for a large area of 300^2 km^2 centered at the SGP central facility, this forcing is still applicable to our LES domain 28.8^2 km^2 due to our case selection criteria that shallow cumulus clouds develop homogeneously in a vast area around SGP without the influence of synoptic-scale weather patterns in the area. In this study, we use the analysis fields of horizontal advective tendency of temperature and specific humidity together with its large-scale subsidence rate to determine the total advective tendency that forces the LES. This allows temperature and moisture vertical advection to depend on the profiles of temperature and moisture simulated by the LES (**?**).

Figure 4 shows the large-scale horizontal advective tendencies, subsidence rate and wind fields of the CASS composite case. Because the forcing contains random error which persists even in the average, we simplify the forcing in order to retain the most important structures of the large

scale advective tendencies while discarding features not statistically significant. First, we perform significance tests to identify whether the composite average data is statistically different from zero at a confidence level of 99%; we then only retain the significant features and smooth the remaining data. For instance, the slight warming in the early morning hours near the surface is found to be no different from zero; from this, we conclude that it is not important and we eliminate it. The constructed horizontal temperature advection (top right panel in Figure 4) generally weakly cools the middle troposphere in the morning and the boundary layer in the late afternoon. The magnitude of this afternoon cooling (1.5 to 3 K day^{-1}) is comparable with the case of ARM97 (**?**), which was 2–4 K day^{-1}. Horizontal moisture advection is only significant before 0800 LST in the boundary layer. The magnitude of morning moistening is consistent with ARM97, which was 2 g kg^{-1} day^{-1} from 0530 to 0830 LST.

Surface fluxes can have a major influence in the calculated forcing because on fair-weather days they are the major component in the column heat budget. However, in the current version of continuous forcing data, the surface energy constraint does not include ECOR data. Since ECOR fluxes have a systematically lower evaporative fraction relative to the EBBR fluxes, the resulting large scale subsidence rate is overestimated. An offline preliminary test shows that the inclusion of ECOR data into the variational analysis will reduce the subsidence rate by 30 to 50 % compared to the original continuous forcing without ECOR data (not shown). With this consideration, we systematically lowered the subsidence rate from the continuous forcing value by 30%. When new continuous forcing data utilizing the combined EBBR and ECOR data becomes available, we will update our CASS composite case avoiding the need for this ad-hoc adjustment.

Figure 4 shows that the large scale subsidence dominates the lower troposphere on our selected days and maximizes around 800 hPa at 1500 LST. The large scale subsidence affects the vertical advection of temperature and moisture. In our case, the strong subsidence induces warming with

a maximum of 3.5 K day^{-1} around 700 hPa. The peak subsidence drying is 3.5 g kg^{-1} day^{-1} just above 850 hPa from 1400 to 1800 LST. In ARM97 there is no specified subsidence. The total advection tendency of moisture in ARM97 shows the drying of about 2 to 4 g kg^{-1} day^{-1} in the lowest 1 km from 1430 to 1730 LST.

In the lower troposphere below 700 hPa, horizontal winds blow from the southwest and turn to the southeast in the afternoon. The composite wind field used for LES is not the simple multi-day average of zonal and meridional winds as the wind direction change and the wind shear might not be represented adequately. Rather the direction is determined from the average zonal and meridional wind, but the wind magnitude is adjusted to reproduce the average wind speed. By doing so, we preserve wind energy and wind shear, and thus reduce the impact on turbulence from composite averaging.

4. Evaluation of LES with observed thermodynamics and cloud statistics

a. General comparison

Figure 5 shows the vertical profiles of LES domain mean potential temperature and water vapor mixing ratio compared with composite soundings at 1130 and 1730 LST. In order to preserve the inversion structure, composite soundings are averaged on a vertical axis of height relative to mixed-layer top and then rescaled by the average mixed-layer height over all days. In general, the LES mixed layer depth agrees well with the observations, e.g. 1.3 km at 1130 LST and 1.8 km at 1730. However, the LES simulated thermodynamics from bin and bulk microphysics is cooler in both the mixed layer and the free troposphere, drier in the mixed layer and moister just above the mixed layer. At 1130 LST, the potential temperature difference is about 0.5 K below 4 km and the mixing ratio difference is 0.25 g kg^{-1} in the mixed layer. At 1730 LST, the LES potential

temperature is almost the same as the observed in the mixed layer but is about 2 K cooler in the free troposphere. Below 1 km, the LES is about 0.5 g kg^{-1} drier than the observed, however between 2 to 3 km, the LES is about 1 g kg^{-1} moister than the observed.

Figure 6 shows the vertical profiles from LES at 1330 LST, the time of maximum cloud fraction. LES cloud fraction is defined as the fraction of grids with a nonzero liquid water content and cloud-averaged fields are just averages over these cloudy grids (**?**). Although the domain mean thermodynamic field is almost the same, the maximum cloud fraction near cloud base from bin microphysics is about 14% compared to 8% from bulk microphysics. Both simulations underestimate the observed cloud fraction at the cloud base level. The in-cloud liquid water content increases almost linearly with cloud vertical extent and reaches 1.2 g m^{-3} at the cloud top in bulk microphysics, while in bin microphysics, it increases only near the cloud base and has an almost constant value of 0.3 g m^{-3} in the whole cloud layer above.

Figure 7 shows a comparison of cloud macrophysical properties from LES with long-term observed statistics. In general, the LES captures the diurnal variation of shallow cumulus exhibited by the observations, especially for the rising cloud base altitude (Figure 7c). However, the LES underestimates the total projected cloud fraction for all clouds (Figure 7a) and clouds with depth greater than 300 meters (Figure 7b), and the cloud chord length (Figure 7d). The LES shows sensitivity to the choice of microphysics. The LES maximum total cloud fraction increases from 22% to 29% when switching from the bulk to bin microphysics (Figure 7a). The total cloud fraction from LES with bin microphysics increases faster than observed in the morning, reaches its maximum value between 1130 LST and 1300 LST and then decreases, whereas the observation shows continuous increases until 1330 LST and then decreases. The area fraction covered by clouds greater than 300 meters in depth almost doubles when bin microphysics is used – 15% versus 7% – however even so, the diurnal maximum is still lower than the observed value of 25% (Figure 7b).

The cloud chord length also increases significantly with bin microphysics scheme; for example, at 1330 LST the cloud chord length increases from 500 m to 850 m, although this is still less than the observed cloud chord length of 1 km (Figure 7d). Overall we can say that while some improvement comes from using bin microphysics, LES clouds tend to be smaller in horizontal and vertical extent than observed.

The lack of cloud is further verified with lower than observed liquid water path and weaker than observed surface shortwave cloud radiative effect (downward shortwave difference between clear sky and the whole sky, Figure 7e, h). Here it is interesting that the effect on radiation is almost the same between the two LES despite the improved cloud macrophysics of the simulation with bin microphysics. This results from the compensation in the bin LES of taller and wider clouds with clouds of lower liquid water content (Fig. 6), such that the domain mean liquid water paths are nearly identical. On the other hand, when comparing the area where cloud liquid water path is greater than 80 g m^{-2}, LES has doubled the observed value (Figure 7f). It is hard to reconcile this result with those of the other comparisons; but it appears to suggest that the in-cloud liquid water content is too large on average.

Further differences between bulk and bin LES are revealed in Figure 8. With bin microphysics, the LES produces more clouds with larger vertical extent, however the condensate in the clouds is smaller compared with bulk microphysics simulation at the same height level. In Fig. 6 the liquid water content from Bin scheme is close to 0.3 g m^{-3}. Furthermore, the in-cloud updraft is weaker. From a scatter plot of 10-second ARSCL cloud depth versus 30-second MWRRET LWP data, we find that for cloud depths up to 800 m, the in-cloud LWP increases almost linearly with cloud depth consistent with an average in-cloud liquid water content of approximately 0.1 g m^{-3} (**?**). The cloud water content from the ARM Cloud Retrieval Ensemble Dataset (ACRED, **?**) also shows the retrieved in-cloud liquid water content to range from 0.03 to 0.15 g m^{-3} (**???**). Overall, these

retrieved values hint at a better simulated but still overestimated cloud condensate from the LES with bin microphysics.

The differences from microphysics are considerable but were often not emphasized in previous LES studies of shallow cumulus. The bulk microphysics is an "all-or-nothing" scheme, in which when there is supersaturation, sufficient water vapor condenses in one time step to eliminate supersaturation; likewise, when there is subsaturation, sufficient cloud water, if available, evaporates within one time step to eliminate subsaturation. It is a well known fact that bulk microphysics often overestimates the evaporation rate as compared with bin microphysics in which droplet size distribution is more realistically represented (**?**). The bin microphysics allows supersaturation and water vapor condenses within a finite time scale (1-10 second for droplets, **?**), and the same for cloud liquid evaporation. The slower evaporation time scale might be a reason for the larger cloud fraction with the bin scheme. Furthermore, as an air parcel rises above its lifting condensation level, the condensational latent heat will be released more gradually in the bin simulation causing a more gradual increase in parcel buoyancy. Thus while the updraft velocity may be the same for air parcels at cloud base, the increase above cloud base may occur at a slower pace with bin microphysics (Fig. 8, third row, see also Fig.10). Since the updraft may be weaker and the cloud size is bigger (Figure 7d) for the bin microphysics, the core area, defined as the updraft cloud area with positive buoyancy, may be much less susceptible to lateral entrainment mixing (**?**) and may penetrate deeper with more gradual but continuous condensational latent heating (Fig. 8, fourth row). This speculation as to why the choice of microphysics affects the simulated clouds will require further investigation.

b. Observational uncertainty

In making judgements about the realism of the LES clouds, one must consider observational uncertainty. Compared to the other cloud quantities presented in this paper, the cloud base height and total vertically projected cloud fraction are the most reliably observed quantities due to the high sensitivity of the ceilometer in detecting the altitude and occurrence of a cloud base. Even so the ceilometer can miss very small clouds of thickness below 100 m (**?**). Thus the actual total cloud fraction might be still slightly higher than shown. The observed cloud chord length was calculated as the duration of the continuous occurrence of a cloud base multiplied by the wind speed measured by wind profilers. This calculation makes use of the frozen turbulence assumption. Although the fixed vertical-pointing instrument may not always measure the center area of clouds, our use of multi-day data and large samples should significantly lower the uncertainty and still give a good representation of cloud size. For LES, snapshot data are used to determine cloud size as the mean horizontal distance in zonal and meridional dimensions covered by contiguous clouds.

The largest uncertainty in cloud statistics is associated with cloud top; such uncertainty affects the area fraction with cloud depth greater than 300 meters (Fig. 7b). Cloud top is determined only from cloud radar echoes above the cloud base, as the lidar and ceilometer signals are attenuated by the cloud before reaching cloud top. At SGP, insect returns above cloud base are hard to distinguish from real clouds with the radar, and in ARSCL data, this distinguishing is often done manually (**??**). Thus sometimes clear air above the cloud that contains insects is mistakenly classified as cloud, which leads to an overestimation in the altitude of cloud top and the cloud vertical extent. Based on this, the actual difference between LES and observation for the area fraction with cloud depth greater than 300 meters might not be as large as shown in Fig. 7b.

Liquid water path is measured by a microwave radiometer (MWR), which is known for its poor performance for thin low-level clouds, such as are common for ShCu. The uncertainty in an individual measurement may be up to 20 g m^{-2} and a well-known issue of the 2-channel MWR retrieval are the non-zero LWP values for clear-sky (e.g. non-zero values before 8 a.m. in Figure 7e). The in-cloud average value of LWP is about 80 g m^{-2} at diurnal maxima on active shallow cumulus days. These LWP retrievals for ShCu come with a significant degree of uncertainty (**??**). In addition, the field of view of MWR is about 5.9^0 degrees which suggests that at the cloud base level, the measuring area could be as large as 200^2 m^2 for 30-second data considering the horizontal wind speed of 7 m s^{-1}. Clouds may partially fill this area and the observed value is an average of much larger area than the grid size of LES, which might be a reason for the model-observation difference shown in Fig. 7f. To test this hypothesis, we calculate the mean LES LWP over an area of 200^2 m^2 surrounding cloudy grid points. However it does not change the LES area fraction with LWP greater than 80 g m^{-2} in Figure 7f. Thus this partial beam filling issue can not explain the difference between LES and observation in Figure 7f.

c. Model sensitivities

To explore the robustness of differences of LES with observations, we have performed a large number of sensitivity tests, in addition to the choice of microphysics. These are more fully described in Appendix (Section A2) but we summarize pertinent results here (Fig. 11 and 12). Sensitivity tests illustrate that LES results are rather insensitive to domain sizes but slightly sensitive to resolution changes. Specifically, LES using bulk microphysics with domain sizes of 57.6^2 km^2, 28.8^2 km^2 and 14.4^2 km^2 and default resolutions produce almost identical total projected cloud fraction. If the horizontal resolution changes from 100 m to 50 m to 25 m, the LES total projected cloud fraction increases from 20% to 22% to 24%. Similarly if vertical resolution increases from

45 m to 20 m to 10 m in lowest 5 km while keeping the default horizontal resolution, the LES total projected cloud fraction increases from 20% to 22% to 25%. The systematic LES underestimate of cloud fraction also appears robust with respect to uncertainties in forcing data. We have also run LES with bulk microphysics for every individual day (Fig. 13) in our case library (Section A3), and while LES produces shallow cumulus clouds on 66% of days, the underestimate of the total cloud fraction is present on almost every day of shallow cumulus.

The persistent discrepancy in cloudiness between LES and observations leads us to speculate about factors we have not tested. In particular, three dimensional radiative transfer was not performed, perhaps contributing to a shortwave cloud effect smaller than the observed. Other missing aspects include a lack of surface flux heterogeneity and interactive land-surface models.

5. Evaluation of LES with observed vertical velocity and mass flux

Cloud-scale vertical velocity and convective mass flux are key diagnostics of convection and the essentials of convection parameterization in many large-scale models. Here, we compare vertically pointing cloud radar retrievals of vertical velocity and mass flux with our LES.

a. What to compare?

Due to considerations of radar sensitivity and insect contamination, comparison of observations to LES requires great caution. In particular, vertical velocity retrievals are performed on a subset of cloudy profiles, and probability of a retrieval increases strongly with liquid water path. Figure 9 shows that the probability distribution of liquid water path as a function of time of day, and the corresponding cumulative probability for a 10-second radar observed profile to be qualified for a valid retrieval of vertical velocity as a function of liquid water path. For instance, Figure 9 shows that at 10 LST, among all the radar profile observations with liquid water path greater

than 30 g m^{-2}, only about 50% have a valid retrieval of vertical velocity in clouds; however the probability of a vertical velocity retrieval for profiles with LWP greater than 80 g m^{-2} increases up to 95%. Therefore, we will use a in-cloud liquid water path of 80 g m^{-2} as a threshold to select data points from both radar observations and LES for vertical velocity and mass fluxes, in order to avoid sampling LES cloudy profiles which would rarely be used by the radar retrieval algorithm.

Figure 10 shows the comparison between LES and radar retrieval at 1330 LST at the time of peak cloud fraction. The top row illustrates calculations that are limited to cloudy profiles with liquid water path of 80 g m^{-2} and greater. The bottom row shows calculations without this restriction using all valid retrievals and all cloudy profiles from the LES. Comparing the two rows, the observed updraft and downdraft area fractions in the bottom increase only about 40% while LES values more than double. This is consistent with the fact that the retrieval algorithm generally does not work in clouds with low liquid water path. For a cloud with liquid water content of 0.1 g m^{-3}, 80 g m^{-2} corresponds to a cloud vertical extent of 800 m. Thus the restriction to cloudy profiles with LWP greater than 80 g m^{-2} excludes cloud edge regions or thin clouds in order to focus on an active ShCu cloud core region.

b. Updraft and downdraft

In the top row of Figure 10, the LES and radar data show comparable updraft and downdraft vertical velocities that increase with height. However, the updraft velocity in LES is stronger than observed – 1.5 m s^{-1} compared to 1 m s^{-1} just above 2000 m where the updraft fraction peaks. Furthermore the updraft is stronger in the LES with bulk microphysics; for example, at 3000 meters, the bulk LES updraft velocity is 3 m s^{-1} versus 2 m s^{-1} in bin microphysics. In both LES and radar data in the top row, the downdraft fraction occupies a significant area compared with updraft fraction. In the radar data, the downdraft maximum area is 1% versus 2% for the updraft.

In the LES with bin microphysics, these numbers are 2% versus 4%. The updraft fraction peaks just above cloud base in both LES and observations. However, the LES downdraft fraction peaks at middle levels in the clouds similar to the observed. The large downdraft fraction leads to non-negligible downdraft mass flux; for example, with the bin LES the downdraft mass flux maximum value is 0.02 m s^{-1}, about 30% of the updraft mass flux whose maximum value is 0.07 m s^{-1}. This behavior is also true when the whole cloudy area is considered (bottom row). Specifically, in the bin LES the downdraft fraction peaks at 4.5%, about 1/2 of the updraft peak of 9%, and the downdraft flux maximizes at 0.045 m s^{-1}, more than 1/3 of the updraft value of 0.11 m s^{-1}. A comparison of the top and bottom rows suggests that cloudy profiles with 80 g m^{-2} or greater liquid water path represent more than 1/3 of the in-cloud updraft area (maximum values of 4% in top plot versus 9% in bottom plot in the bin LES) and in-cloud downdraft area (maximum values of 1.7% in top versus 4.5% in bottom). Furthermore these cloudy profiles carry more than 60% of the updraft mass flux (maximum values of 0.07 m s^{-1} in top versus 0.11 m s^{-1} in bottom) and more than 40% of the downdraft mass flux (maximum values of 0.02 m s^{-1} in top versus 0.045 m s^{-1} in bottom). Interestingly, the ratio of downdraft area (or flux) to updraft area (or flux) is significantly smaller in the bulk LES; if the observed ratio is to be trusted despite of the underestimated updraft/downdraft fraction in retrieval data due to insect contamination and radar sensitivity, the comparison suggests that the bin LES have more realistic cloud dynamics. Overall, it is worth noting that the non-negligible downdraft in-cloud area fraction and mass flux in our case differs from oceanic shallow cumulus studies (**?**), in which the downdrafts are found usually outside of clouds (**?**) and the in-cloud downdraft is very minor compared to in-cloud updraft (**?**).

6. Summary

Based on 13 years of observational data at the ARM SGP site, we have constructed case libraries for different convective regimes: active and forced fair-weather shallow cumulus (**?**), and shallow cumulus that develops into late-afternoon deep convection (**?**). This study focuses on active shallow cumulus, for which we have constructed a new composite case called CASS relying heavily upon observations. Through this new case, we hope to connect all together: observations, LES and in the future, a single-column version of GCM for parameterization development.

This case aims to represent a pure land-surface driven diurnal cycle of shallow cumulus that is sensitive to local temperature and humidity conditions. There is a prevailing well-developed continental non-precipitating shallow cumulus case (ARM97) which has been widely used in cloud modeling studies. However, the ARM97 case was not completely typical of surface-forced shallow cumulus due to an initial cloud present in the early morning. In addition, ARM97 used very few actual cloud observations. It is only by constructing a new case that we can get a case typical of surface-driven shallow cumulus and for which we can use the observations from the advanced instrumentation that ARM has installed in the 20 years since the date of the ARM97 case.

The new composite case consists of forcing data based on long-term sounding, surface heat fluxes and continuous variational analysis of the ARM SGP site measurements. For initial conditions, the early-morning initial profile incorporates a residual layer resulting from the previous day's mixed layer, a very common behavior of atmospheric boundary layer almost on every ShCu day. As a result, the simulated cloud onset time improves by shifting to one hour earlier. For boundary conditions, because no single station nor single instrument data characterizes the domain mean surface heat fluxes and evaporative fraction accurately, cloud base is best simulated using a constrained total surface heat flux and an average of evaporative fraction measured over

different land types. For large-scale forcing, we disregard the values not statistically significant and simplify the forcing pattern to retain the essence of average large-scale advective tendencies and subsidence rate. All these steps are taken to keep the case consistent with the observations while at the same time keeping the case as simple as possible to represent the local atmospheric and surface conditions on a typical surface-forced shallow cumulus days.

LES results for the composite case are evaluated against observed cloud statistics, such as total surface projected cloud fraction, cloud fraction with vertical extent greater than 300 meters, cloud base height and cloud chord length. Overall, both LES we present exhibit a good comparison with observation, particularly for the diurnal evolution of cloud base altitude. This leads credence to the case that we have constructed. Despite this, both LES illustrate an underestimate in the amount of cloud and its radiative impact. This bias is particularly robust and LES show little sensitivities to case construction or model configuration options such as grid resolution or domain size. The largest model sensitivity we have found is to the choice of microphysics. Compared with the default bulk 1-moment microphysics scheme, the LES with spectral bin microphysics improves somewhat the underestimated total cloud fraction and area fraction of clouds with vertical extent greater than 300 meters. The LES with bin microphysics shows weaker in-cloud vertical motion and smaller in-cloud condensate. We speculate that these changes are the result of a more realistic representation of supersaturation and droplet size distribution driven by a finite time scale of condensation and evaporation that causes clouds to linger longer. With a larger cloud fraction, updrafts are more protected from entrainment leading to a taller clouds. The condensational heat release is more gradual leading to less in-cloud condensate.

The LES are further compared to radar retrievals of vertical velocity and mass fluxes. Due to radar sensitivity and retrieval algorithm limitations, the fairest comparison is limited to cloudy profiles with liquid water path greater than 80 g m^{-2}. The LES exhibit downdraft velocities that

are comparable to observations but have a slightly stronger updrafts. In both observation and LES, velocities increase with height. Both LES have a larger updraft area and a larger updraft mass flux, approximately double that observed. Both LES and radar retrievals show a significant portion of the cloudy columns with LWP>80 g m^{-2} is occupied by downdrafts – 25% or more. This leads to non-negligible downdraft mass flux inside the clouds. This downdraft behavior is different from that of oceanic shallow cumulus in which the downdraft mainly happens in the immediate vicinity outside of the cloud (**???**).

It may be worth bearing in mind that this case is well designed to represent mid-latitude surface-driven non-precipitating shallow cumulus at the US Southern Great Plains. Our case might not apply to convection over other continental regions, such as the Amazon with its dense vegetation coverage and stronger surface latent fluxes or the African Monsoon region with much stronger surface sensible heat flux or Cabauw, a mid-latitude region with higher evaporative fraction but a colder and drier boundary layer (**?**) .

In summary, a new composite LES case called CASS is successfully developed to represent the typical fair-weather non-precipitating shallow cumulus clouds over the SGP whose life cycle is mainly driven by land-surface forcing. The CASS case is well constrained by observations and LES show some sensitivity to different microphysics schemes. In the future, we will systematically test the sensitivity of this case to local environmental conditions such as atmospheric moisture and stability, evaporative fraction and surface heterogeneity. We will also compare LES to the new observations of sub-cloud vertical velocity from the Doppler Lidar as well as surface heterogeneity from the new SGP facilities ARM has established (**?**). The CASS case will also be used for testing single-column versions of climate models with newly developed boundary layer mixing and convection parameterizations.

Acknowledgments. The authors sincerely thank Marat Khairoutdinov, Peter Blossey, Robert Pincus and Takanobu Yamaguchi who originally developed SAM and contributed significant improvement to the code. We thank Anning Cheng, Kuan-Man Xu, Thijs Heus and Chris Bretherton for their suggestions and discussions on this work. We thank Chris Golaz for his comments on the manuscript. We thank Patrick Minnis's NASA Langley group, David Doelling from NASA/Langley, and Andrew Heidinger from NOAA/NESDIS for discussions and providing GOES satellite images for our case selections. We sincerely thank three anonymous reviewers and the Editor Wojciech Grabowski for their constructive comments to improve the manuscript. Data from the U.S. Department of Energy (DOE) as part of the Atmospheric Radiation Measurement (ARM) Climate Research Facility Southern Great Plains site were used. This work was supported by Atmospheric Systems Research (ASR) program and ARM program in Office of Biological and Environmental Research, Office of Science, DOE. Lawrence Livermore National Laboratory is operated for the DOE by Lawrence Livermore National Security, LLC under Contract DE-AC52-07NA27344.

APPENDIX

A1. CASS access

CASS stands for Continental Active Surface-forced Shallow cumulus. Please visit http://portal.nersc.gov/project/capt/CASS/ to download the forcing data for the composite case. Through this website, successive version of CASS will be released. These improved versions are anticipated to include updates of the forcing data according to the ARM data changes on initial sounding, surface heat fluxes and continuous forcing based on variational analysis. We will also release input data needed to drive the land surface scheme once it is ready. In addition, information on the observed cloud statistics, composite soundings, the sensitivity tests and the ensemble runs are also available online and data is upon request to the first author. The composite case is built upon a case library from year 1997 to 2009. We are actively extending this case library for CASS to the most recent years together with observational statistics from new instruments at the newly-arranged super site of ARM SGP.

A2. Sensitivity tests

Listed in Table 1, there are 13 independent LES sensitivity experiments with bulk microphysics in which only one model configuration or one forcing uncertainty is changed while other conditions are held the same as in the default control run.

Figure 11 shows the LES bias relative to observed cloud statistics at 1330 LST, the diurnal peak time of the total cloud fraction. In all the cloud statistics except the cloud base, the LES sensitivity runs shows biases of same sign, particularly underestimate of cloud fraction, cloud chord length, liquid water path and radiation at the surface. Although the LES underestimate the cloud area with vertical extent greater than 300 m, the LES tend to overestimate the fraction of much deeper

clouds such as with LWP greater than 80 g m^{-2}. The cloud base height is particularly sensitive to the evaporative fraction and the total heat flux, with the largest biases shown for the LES forced with either the EBBR fluxes alone or the ECOR fluxes alone.

Figure 12 shows the LES bias in the mixed layer potential temperature and mixing ratio relative to the sounding data at 1130 LST and 1730 LST. Through the diurnal evolution, the boundary layer development in potential temperature and mixing ratio is very comparable to sounding data. In the late morning, the boundary layer shows a cold bias about 0.6 K for all the sensitivity runs except experiment 11 in which large-scale forcing retains the small values that are not significant different from zero. In this experiment, including these small tendencies in temperature field leads to slightly warm bias in late morning. In the late afternoon, the cold bias almost diminishes in most of the sensitivity runs while the warm bias in experiment 11 grow as big as 0.55 K. The slight dry bias about 0.2 g kg^{-1} in the morning grows to about 0.6 g kg^{-1} in the late afternoon.

Among all the sensitivity runs, bin microphysics LES run shows more superiority in simulating total projected cloud fraction, cloud area fraction with the cloud vertical extent greater than 300 m and cloud chord length. Compared with other model configurations or forcing uncertainty, the control run with bulk microphysics shows slight superiority in simulating cloud base height, domain mean liquid water path and very comparable statistics in other cloud properties and boundary layer thermodynamics.

A3. Ensemble of golden days

In addition to sensitivity tests, we take the ensemble approach in which many ShCu days of LES are forced individually. There are totally 76 days in our shallow cumulus case library. Due to missing data of either sounding or large-scale forcing, we have 62 days for valid LES runs. For each day, we reduce the large-scale subsidence rate by 30% as was done in the composite

case. The initial soundings at 0530 LST on individual days often exhibit a residual layer or even multiple mixed-layers above the stable layer near the surface. From the LES of these 62 days, only on 40 days does the LES produce shallow cumulus while on the other 22 days quite different weather regimes are produced: 2 days of clear sky, 10 days of single layer overcast stratiform clouds and another 10 days of multi-layered clouds. This indeed reflects the fact that although each golden day case is observed to have shallow cumulus, uncertainties and random errors in the initial conditions, surface fluxes and large-scale forcing may contribute to a failure in the LES.

Figure 13 shows the comparison between the LES of the composite case and the ensemble runs of 40 days of shallow cumulus. Although there is quite a spread in the cloud statistics due to day-to-day variability (as shown by the interquartile range of the ensemble runs), the general behavior of the whole ensemble and especially the ensemble mean is very similar to the LES simulation for the composite case. The ensemble mean shows a consistent underestimation of total cloud fraction, cloud area with vertical extent greater than 300 m and cloud horizontal extent such as chord length and in the surface longwave radiation and shortwave cloud radiative effect. The ensemble still shows overestimate in the area fraction with clouds whose liquid water path is greater than 80 g m^{-2}.

Despite the similarities, there are some small but statistically significant differences between the ensemble mean and the composite case. For example, the liquid water path of ensemble mean is significantly greater than the LES simulation of the composite case except at the diurnal peak time of 1330 LST. These differences may reflect a small non-linearity of LES responses to forcings. In other words, the ensemble mean behavior resulting from individual day forcings is not necessarily the same as the LES result of the composite case driven by the mean forcing. Another possible cause of the small differences is that the ensemble of 40 days of shallow cumulus LES runs is a subset of all the observed shallow cumulus days which constitute the composite

case. As such, the forcing of the composite case consists of contributions from all the cases including those do not produce shallow cumulus clouds in the individual LES runs. With this difference in the forcing, even if the LES response to forcing is linear, there might be differences between the ensemble mean and the composite case. Still we emphasized that all differences with the observations are the same for the ensemble mean and the composite case. This gives us the confidence that the composite case may represent the average behavior of SGP surface-forced shallow cumulus days and will be appropriate to serve as a good case for both LES tests and climate model parameterization studies.

References

Angevine, W. M., H. Jiang, and T. Mauritsen, 2010: Performance of an eddy diffusivity–mass flux scheme for shallow cumulus boundary layers. *Mon. Wea. Rev.*, **138 (7)**, 2895–2912, doi: 10.1175/2010MWR3142.1, URL http://dx.doi.org/10.1175/2010MWR3142.1.

Berg, L. K., and E. I. Kassianov, 2008: Temporal variability of fair-weather cumulus statistics at the ACRF SGP site. *J. Climate*, **21**, 3344–3358.

Betts, A. K., M. Köhler, and Y. Zhang, 2009: Comparison of river basin hydrometeorology in ERA-Interim and ERA-40 reanalyses with observations. *J. Geophys. Res. Atmos.*, **114**, d02101, doi:10.1029/2008JD010761.

Bogenschutz, P. A., A. Gettelman, H. Morrison, V. E. Larson, C. Craig, and D. P. Schanen, 2013: Higher-order turbulence closure and its impact on climate simulations in the community atmosphere model. *J. Climate*, **26 (23)**, 9655–9676, doi:10.1175/JCLI-D-13-00075.1, URL http://dx.doi.org/10.1175/JCLI-D-13-00075.1.

Bogenschutz, P. A., A. Gettelman, H. Morrison, V. E. Larson, D. P. Schanen, N. R. Meyer, and C. Craig, 2012: Unified parameterization of the planetary boundary layer and shallow convection with a higher-order turbulence closure in the community atmosphere model: single-column experiments. *Geosci. Model Dev.*, **5 (6)**, 1407–1423, doi:10.5194/gmd-5-1407-2012, URL http://www.geosci-model-dev.net/5/1407/2012/.

Bogenschutz, P. A., and S. K. Krueger, 2013: A simplified pdf parameterization of subgrid-scale clouds and turbulence for cloud-resolving models. *J. Adv. Model. Earth Syst.*, **5 (2)**, 195–211, doi:10.1002/jame.20018, URL http://dx.doi.org/10.1002/jame.20018.

Brown, A. R., and Coauthors, 2002: Large-eddy simulation of the diurnal cycle of shallow cumulus convection over land. *Quart. J. Roy. Meteor. Soc.*, **128**, 1075–1093.

Chandra, A. S., P. Kollias, and B. A. Albrecht, 2013: Multiyear summertime observations of daytime fair-weather cumuli at the arm southern great plains facility. *J. Climate*, **26 (24)**, 10 031–10 050, doi:10.1175/JCLI-D-12-00223.1, URL http://dx.doi.org/10.1175/JCLI-D-12-00223.1.

Cheng, A., and K.-M. Xu, 2015: Improved low-cloud simulation from the community atmosphere model with an advanced third-order turbulence closure. *J. Climate*, **28 (14)**, 5737–5762, doi:10.1175/JCLI-D-14-00776.1, URL http://dx.doi.org/10.1175/JCLI-D-14-00776.1.

Clothiaux, E., and Coauthors, 2001: *The ARM Millimeter Wave Cloud Radars (MMCRs) and the Active Remote Sensing of Clouds (ARSCL) Value Added Product (VAP)*. DOE Tech. Memo. ARM VAP-002.1, U.S. Department of Energy, Washington, D.C.

Clothiaux, E. E., T. P. Ackerman, G. G. Mace, K. P. Moran, R. T. Marchand, M. Miller, and B. E. Martner, 2000: Objective determination of cloud heights and radar reflectivities using a combination of active remote sensors at the ARM CART sites. *J. Appl. Meteor.*, **39**, 645–665.

Clough, S., M. Shephard, E. Mlawer, J. Delamere, M. Iacono, K. Cady-Pereira, S. Boukabara, and P. Brown, 2005: Atmospheric radiative transfer modeling: a summary of the AER codes. *J. Quant. Spectrosc. Radiat. Transfer*, **91 (2)**, 233 – 244, doi:http://dx.doi.org/10.1016/j.jqsrt.2004.05.058, URL http://www.sciencedirect.com/science/article/pii/S0022407304002158.

Dawe, J. T., and P. H. Austin, 2012: Statistical analysis of an les shallow cumulus cloud ensemble using a cloud tracking algorithm. *Atmospheric Chemistry and Physics*, **12 (2)**, 1101–1119, doi:10.5194/acp-12-1101-2012, URL http://www.atmos-chem-phys.net/12/1101/2012/.

de Roode, S. R., A. P. Siebesma, H. J. J. Jonker, and Y. de Voogd, 2012: Parameterization of the vertical velocity equation for shallow cumulus clouds. *Mon. Wea. Rev.*, **140 (8)**, 2424–2436, doi:10.1175/MWR-D-11-00277.1, URL http://dx.doi.org/10.1175/MWR-D-11-00277.1.

Dong, X., P. Minnis, and B. Xi, 2005: A climatology of midlatitude continental clouds from the ARM SGP Central Facility. Part I: Low-level cloud macrophysical, microphysical and radiative properties. *J. Climate*, **18**, 1391–1410.

Endo, S., and Coauthors, 2015: Racoro continental boundary layer cloud investigations. part ii: Large-eddy simulations of cumulus clouds and evaluation with in-situ and ground-based observations. *J. Geophys. Res. Atmos.*, n/a–n/a, doi:10.1002/2014JD022525, URL http://dx.doi.org/10.1002/2014JD022525.

Fan, J., M. Ovtchinnikov, J. M. Comstock, S. A. McFarlane, and A. Khain, 2009: Ice formation in arctic mixed-phase clouds: Insights from a 3-d cloud-resolving model with size-resolved aerosol and cloud microphysics. *J. Geophys. Res. Atmos.*, **114 (D4)**, n/a–n/a, doi:10.1029/2008JD010782, URL http://dx.doi.org/10.1029/2008JD010782, d04205.

Gentine, P., A. K. Betts, B. R. Lintner, K. L. Findell, C. C. van Heerwaarden, and F. D'Andrea, 2013a: A probabilistic bulk model of coupled mixed layer and convection. part ii: Shallow convection case. *J. Atmos. Sci.*, **70 (6)**, 1557–1576, doi:10.1175/JAS-D-12-0146.1, URL http://dx.doi.org/10.1175/JAS-D-12-0146.1.

Gentine, P., A. A. M. Holtslag, F. D'Andrea, and M. Ek, 2013b: Surface and atmospheric controls on the onset of moist convection over land. *J. Hydrometeor.*, **14 (5)**, 1443–1462, doi:10.1175/JHM-D-12-0137.1, URL http://dx.doi.org/10.1175/JHM-D-12-0137.1, http://dx.doi.org/10.1175/JHM-D-12-0137.1.

Golaz, J.-C., V. E. Larson, and W. R. Cotton, 2002: A pdf-based model for boundary layer clouds. part ii: Model results. *J. Atmos. Sci.*, **59 (24)**, 3552–3571, doi:10.1175/1520-0469(2002)059⟨3552:APBMFB⟩2.0.CO;2, URL http://dx.doi.org/10.1175/1520-0469(2002)059⟨3552:APBMFB⟩2.0.CO;2.

Guichard, F., and Coauthors, 2004: Modeling the diurnal cycle of deep precipitating convection over land with cloud-resolving models and single-column models. *Quart. J. Roy. Meteor. Soc.*, **130**, 3139–3172.

Hägeli, P., D. G. Steyn, and K. B. Strawbridge, 2000: Spatial and temporal variability of mixed-layer depth and entrainment zone thickness. *Bound.-Layer Meteor.*, **97**, 47–71.

Heus, T., and H. J. J. Jonker, 2008: Subsiding shells around shallow cumulus clouds. *J. Atmos. Sci.*, **65 (3)**, 1003–1018, doi:10.1175/2007JAS2322.1, URL http://dx.doi.org/10.1175/2007JAS2322.1, http://dx.doi.org/10.1175/2007JAS2322.1.

Hourdin, F., and Coauthors, 2013: Lmdz5b: the atmospheric component of the ipsl climate model with revisited parameterizations for clouds and convection. *Clim. Dyn.*, **40 (9-10)**, 2193–2222, doi:10.1007/s00382-012-1343-y, URL http://dx.doi.org/10.1007/s00382-012-1343-y.

Jakob, C., 2010: Accelerating progress in global atmospheric model development through improved parameterizations: Challenges, opportunities, and strategies. *Bull. Amer. Meteor. Soc.*, **91 (7)**, 869–875, doi:10.1175/2009BAMS2898.1, URL http://dx.doi.org/10.1175/2009BAMS2898.1, http://dx.doi.org/10.1175/2009BAMS2898.1.

Khain, A., A. Pokrovsky, M. Pinsky, A. Seifert, and V. Phillips, 2004: Simulation of effects of atmospheric aerosols on deep turbulent convective clouds using a spectral microphysics mixed-

760 phase cumulus cloud model. part I: Model description and possible applications. *J. Atmos. Sci.*,
761 **61 (24)**, 2963–2982, doi:10.1175/JAS-3350.1, URL http://dx.doi.org/10.1175/JAS-3350.1.

762 Khairoutdinov, M. F., and D. A. Randall, 2003: Cloud resolving modeling of the ARM summer
763 1997 IOP: model formulation, results, uncertainties and sensitivities. *J. Atmos. Sci.*, **30**, 607–
764 625.

765 Lamer, K., and P. Kollias, 2015: Observations of fair-weather cumuli over land: Dynami-
766 cal factors controlling cloud size and cover. *Geophys. Res. Lett.*, **42 (20)**, 8693–8701, doi:
767 10.1002/2015GL064534, URL http://dx.doi.org/10.1002/2015GL064534, 2015GL064534.

768 Lamer, K., P. Kollias, and L. Nuijens, 2015: Observations of the variability of shallow trade
769 wind cumulus cloudiness and mass flux. *J. Geophys. Res. Atmos.*, **120 (12)**, 6161–6178, doi:
770 10.1002/2014JD022950, URL http://dx.doi.org/10.1002/2014JD022950, 2014JD022950.

771 Lenderink, G., and Coauthors, 2004: The diurnal cycle of shallow cumulus clouds over land:
772 A single-column model intercomparison study. *Quart. J. Roy. Meteor. Soc.*, **130**, 3339–3364,
773 doi:10.1256/qj.03.122.

774 Lin, W., and Coauthors, 2015: Racoro continental boundary layer cloud investigations. part iii:
775 Separation of parameterization biases in single-column model cam5 simulations of shallow cu-
776 mulus. *J. Geophys. Res. Atmos.*, n/a–n/a, doi:10.1002/2014JD022524, URL http://dx.doi.org/
777 10.1002/2014JD022524.

778 Long, C. N., and Y. Shi, 2008: An automated quality assessment and control algorithm for surface
779 radiation measurements. *Open Atmos. Sci. J.*, **2**, 23–37.

780 Mace, G. G., and S. Benson, 2008: The vertical structure of cloud occurrence and radiative forcing
781 at the sgp arm site as revealed by 8 years of continuous data. *Journal of Climate*, **21 (11)**, 2591–

2610, doi:10.1175/2007JCLI1987.1, URL http://dx.doi.org/10.1175/2007JCLI1987.1, http://dx.doi.org/10.1175/2007JCLI1987.1.

Mace, G. G., S. Benson, and S. Kato, 2006a: Cloud radiative forcing at the atmospheric radiation measurement program climate research facility: 2. vertical redistribution of radiant energy by clouds. *J. Geophys. Res. Atmos.*, **111 (D11)**, n/a–n/a, doi:10.1029/2005JD005922, URL http://dx.doi.org/10.1029/2005JD005922, d11S91.

Mace, G. G., and Coauthors, 2006b: Cloud radiative forcing at the atmospheric radiation measurement program climate research facility: 1. technique, validation, and comparison to satellite-derived diagnostic quantities. *J. Geophys. Res. Atmos.*, **111 (D11)**, n/a–n/a, doi:10.1029/2005JD005921, URL http://dx.doi.org/10.1029/2005JD005921, d11S90.

Mather, J., 2016: *Decadal Vision Progress Report: Implementation Plans and Status for the Next Generation ARM Facility*. DOE/SC-ARM-16-036.

Mlawer, E. J., S. J. Taubman, P. D. Brown, M. J. Iacono, and S. A. Clough, 1997: Radiative transfer for inhomogeneous atmospheres: RRTM, a validated correlated-k model for the longwave. *J. Geophys. Res. Atmos.*, **102 (D14)**, 16 663–16 682, doi:10.1029/97JD00237, URL http://dx.doi.org/10.1029/97JD00237.

Morrison, H., J. A. Curry, and V. I. Khvorostyanov, 2005: A new double-moment microphysics parameterization for application in cloud and climate models. part i: Description. *J. Atmos. Sci.*, **62 (6)**, 1665–1677, doi:10.1175/JAS3446.1, URL http://dx.doi.org/10.1175/JAS3446.1.

Neggers, R. A. J., M. Köhler, and A. C. M. Beljaars, 2009: A dual mass flux framework for boundary layer convection. part i: Transport. *J. Atmos. Sci.*, **66 (6)**, 1465–1487, doi:10.1175/2008JAS2635.1, URL http://dx.doi.org/10.1175/2008JAS2635.1.

Neggers, R. A. J., and A. P. Siebesma, 2013: Constraining a system of interacting parameterizations through multiple-parameter evaluation: Tracing a compensating error between cloud vertical structure and cloud overlap. *J. Climate*, **26 (17)**, 6698–6715, doi:10.1175/JCLI-D-12-00779.1, URL http://dx.doi.org/10.1175/JCLI-D-12-00779.1.

Neggers, R. A. J., A. P. Siebesma, and T. Heus, 2012: Continuous single-column model evaluation at a permanent meteorological supersite. *Bull. Amer. Meteor. Soc.*, **93 (9)**, 1389–1400, doi:10.1175/BAMS-D-11-00162.1, URL http://dx.doi.org/10.1175/BAMS-D-11-00162.1.

Neggers, R. A. J., A. P. Siebesma, G. Lenderink, and A. A. M. Holtslag, 2004: An evaluation of mass flux closures for diurnal cycles of shallow cumulus. *Mon. Wea. Rev.*, **132 (11)**, 2525–2538, doi:10.1175/MWR2776.1, URL http://dx.doi.org/10.1175/MWR2776.1.

Oue, M., P. Kollias, K. W. North, A. Tatarevic, S. Endo, A. M. Vogelmann, and W. I. Gustafson, 2016: Estimation of cloud fraction profile in shallow convection using a scanning cloud radar. *Geophys. Res. Lett.*, n/a–n/a, doi:10.1002/2016GL070776, URL http://dx.doi.org/10.1002/2016GL070776.

Park, S., and C. S. Bretherton, 2009: The university of washington shallow convection and moist turbulence schemes and their impact on climate simulations with the community atmosphere model. *J. Climate*, **22 (12)**, 3449–3469, doi:10.1175/2008JCLI2557.1, URL http://dx.doi.org/10.1175/2008JCLI2557.1.

Randall, D. A., and D. G. Cripe, 1999: Alternative methods for specification of observed forcing in single-column models and cloud system models. *J. Geophys. Res. Atmos.*, **104 (D20)**, 24 527–24 545, doi:10.1029/1999JD900765, URL http://dx.doi.org/10.1029/1999JD900765.

825 Rio, C., and F. Hourdin, 2008: A thermal plume model for the convective boundary layer: Rep-
826 resentation of cumulus clouds. *J. Atmos. Sci.*, **65 (2)**, 407–425, doi:10.1175/2007JAS2256.1,
827 URL http://dx.doi.org/10.1175/2007JAS2256.1.

828 Rio, C., F. Hourdin, F. Couvreux, and A. Jam, 2010: Resolved versus parametrized boundary-layer
829 plumes. part ii: Continuous formulations of mixing rates for mass-flux schemes. *Bound.-Layer*
830 *Meteor.*, **135 (3)**, 469–483, doi:10.1007/s10546-010-9478-z, URL http://dx.doi.org/10.1007/
831 s10546-010-9478-z.

832 Siebesma, A. P., P. M. M. Soares, and J. Teixeira, 2007: A combined eddy-diffusivity mass-flux
833 approach for the convective boundary layer. *J. Atmos. Sci.*, **64 (4)**, 1230–1248, doi:10.1175/
834 JAS3888.1, URL http://dx.doi.org/10.1175/JAS3888.1.

835 Siebesma, A. P., and Coauthors, 2003: A large eddy simulation intercomparison study of shallow
836 cumulus convection. *J. Atmos. Sci.*, **60**, 1201–1219.

837 Turner, D. D., S. A. Clough, J. Liljegren, E. Clothiaux, K. Cady-Pereira, and K. Gaustad, 2007a:
838 Retrieving liquid water path and precipitable water vapor from Atmospheric Radiation Mea-
839 surement (ARM) microwave radiometers. *IEEE Trans. Geosci. Remote Sens.*, **45**, 3680–3690,
840 doi:10.1109/TGRS.2007.903703.

841 Turner, D. D., and Coauthors, 2007b: Thin liquid water clouds: Their importance and our chal-
842 lenge. *Bull. Amer. Meteor. Soc.*, **88**, 177–190.

843 Twomey, S., 1959: The nuclei of natural cloud formation Part II: The supersaturation in natural
844 clouds and the variation of cloud droplet concentration. *Geofisica pura e applicata*, **43 (1)**,
845 243–249, doi:10.1007/BF01993560, URL http://dx.doi.org/10.1007/BF01993560.

Vilà-Guerau de Arellano, J., 2007: Role of nocturnal turbulence and advection in the formation of shallow cumulus over land. *Quart. J. Roy. Meteor. Soc.*, **133**, 1615–1627, doi:10.1002/qj.138.

Vogelmann, A. M., and Coauthors, 2012: Racoro extended-term aircraft observations of boundary layer clouds. *Bull. Amer. Meteor. Soc.*, **93 (6)**, 861–878, doi:10.1175/BAMS-D-11-00189.1, URL http://dx.doi.org/10.1175/BAMS-D-11-00189.1.

Vogelmann, A. M., and Coauthors, 2015: Racoro continental boundary layer cloud investigations. part i: Case study development and ensemble large-scale forcings. *J. Geophys. Res. Atmos.*, n/a–n/a, doi:10.1002/2014JD022713, URL http://dx.doi.org/10.1002/2014JD022713.

Wang, Y., J. Fan, R. Zhang, L. R. Leung, and C. Franklin, 2013: Improving bulk microphysics parameterizations in simulations of aerosol effects. *J. Geophys. Res. Atmos.*, **118 (11)**, 5361–5379, doi:10.1002/jgrd.50432, URL http://dx.doi.org/10.1002/jgrd.50432.

Xie, S., R. T. Cederwall, and M. Zhang, 2004: Developing long-term single-column model/cloud system resolving model forcing data using numerical weather prediction products constrained by surface and top of the atmosphere observations. *J. Geophys. Res. Atmos.*, **109**, D01104, doi:10.1029/2003JD004045.

Xie, S., and Coauthors, 2010: ARM climate modeling best estimate data. *Bull. Amer. Meteor. Soc.*, **91**, 10.1175/2009BAMS2891.1.

Zhang, M. H., and J. L. Lin, 1997: Constrained variational analysis of sounding data based on column-integrated budgets of mass, heat, moisture, and momentum: Approach and application to arm measurements. *J. Atmos. Sci.*, **54**, 1503–1524.

Zhang, Y., and S. A. Klein, 2010: Mechanisms affecting the transition from shallow to deep convection over land: Inferences from observations of the diurnal cycle collected at the ARM Southern Great Plains site. *J. Atmos. Sci.*, **67**, 2943–2959.

Zhang, Y., and S. A. Klein, 2013: Factors controlling the vertical extent of fair-weather shallow cumulus clouds over land: Investigation of diurnal-cycle observations collected at the arm southern great plains site. *J. Atmos. Sci.*, **70**, 1297–1315, doi:10.1175/JAS-D-12-0131.1.

Zhao, C., and Coauthors, 2012: Toward understanding of differences in current cloud retrievals of arm ground-based measurements. *J. Geophys. Res. Atmos.*, **117 (D10)**, n/a–n/a, doi:10.1029/2011JD016792, URL http://dx.doi.org/10.1029/2011JD016792.

LIST OF TABLES

Sensitivity Tests	
-1	same as 0, except with spectral bin microphysics scheme
0	CASS default control run with bulk microphysics scheme (which is used in all the following experiments)
1	same as 0, except with a quartered domain of 14.4 km by 14.4 km
2	same as 0, except with a quadruple domain of 57.6 km by 57.6 km
3	same as 0, except with a doubled finer horizontal resolution of 25 meter
4	same as 0, except with a half coarser horizontal resolution of 100 meter
5	same as 0, except with a doubled finer vertical resolution of 10 meter below 5 km
6	same as 0, except with a half coarser vertical resolution of 45 meter below 5 km
7	same as 0, except with a constant geostrophic wind 10 m s^{-1}
8	same as 0, except with a wind nudging time scale of 10 hours, 10 times longer than control run
9	same as 0, except with a subsidence rate without ECOR flux correction
10	same as 0, except with an initial sounding without residual layer behavior
11	same as 0, except with large-scale forcing without removing values that are not significantly different from zero
12	same as 0, except with EBBR average surface heat fluxes
13	same as 0, except with ECOR average surface heat fluxes

TABLE 1. List of sensitivity tests on LES configurations and forcing uncertainties.

LIST OF FIGURES

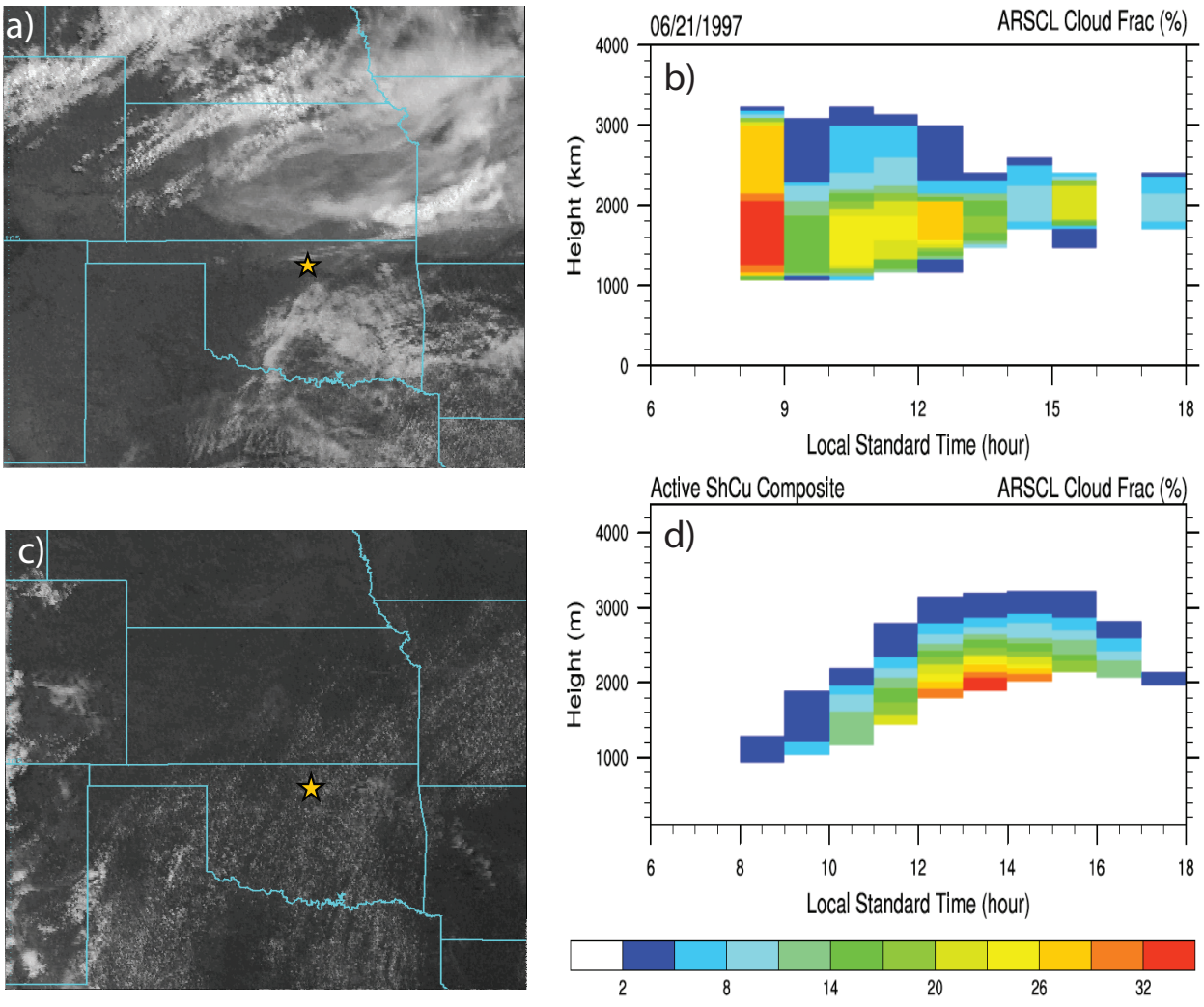

930 FIG. 1. Top left (a): 0.65 μm reflectance by GOES-8 at 08:15 Local Standard Time (LST) on June 21 1997 over ARM SGP site
931 (yellow star denotes the location of central facility). Top right (b): Time versus height plot of vertical cloud fraction (%) based on
932 the vertically pointing radar-lidar-ceilometer combined value added product (ARSCL). X-axis is the LST on June 21 1997. Bottom
933 left (c): same image but for 2001/05/14 at 13:15 LST, one of the shallow cumulus days selected in **??**. Bottom right (d): observed
934 ARSCL time-height profile of cloud fraction for our composite case.

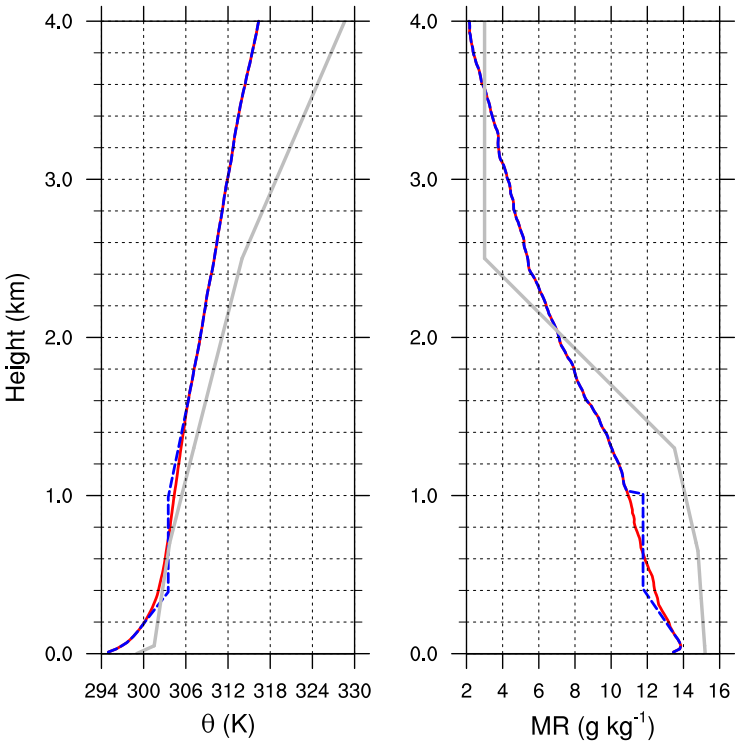

935 FIG. 2. Initial sounding profile at 0530 LST. The redline shows the average sounding over all days used in the composite,
936 while the blue line shows the CASS sounding after imposing a residual layer. The initial sounding for the ARM97 case is denoted
937 by grey solid lines.

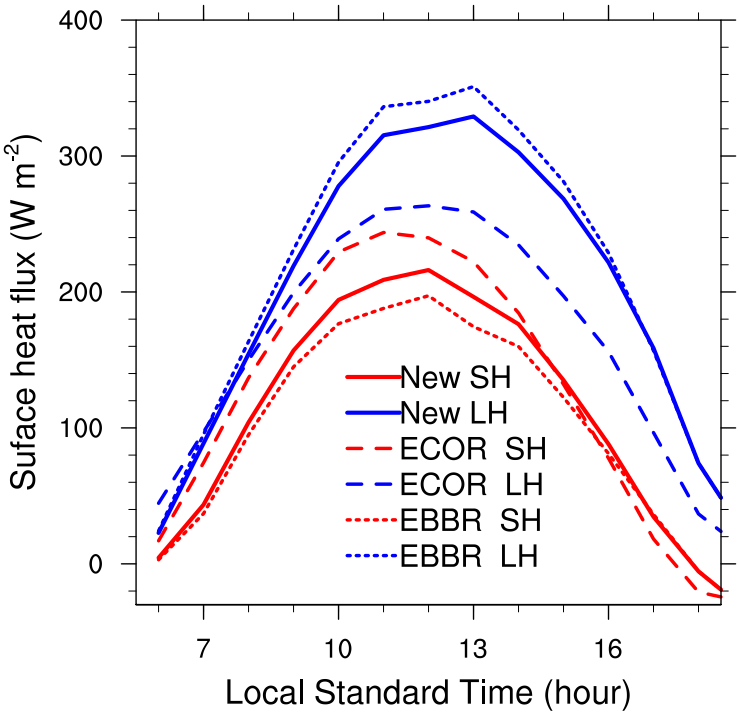

938 FIG. 3. Diurnal cycle of domain-average surface sensible (red) and latent (blue) heat fluxes from EBBR (dotted lines), ECOR
939 (dashed lines) and combined EBBR/ECOR data (solid lines) using total energy flux from EBBR and an average evaporative fraction
940 based on both EBBR and ECOR data.

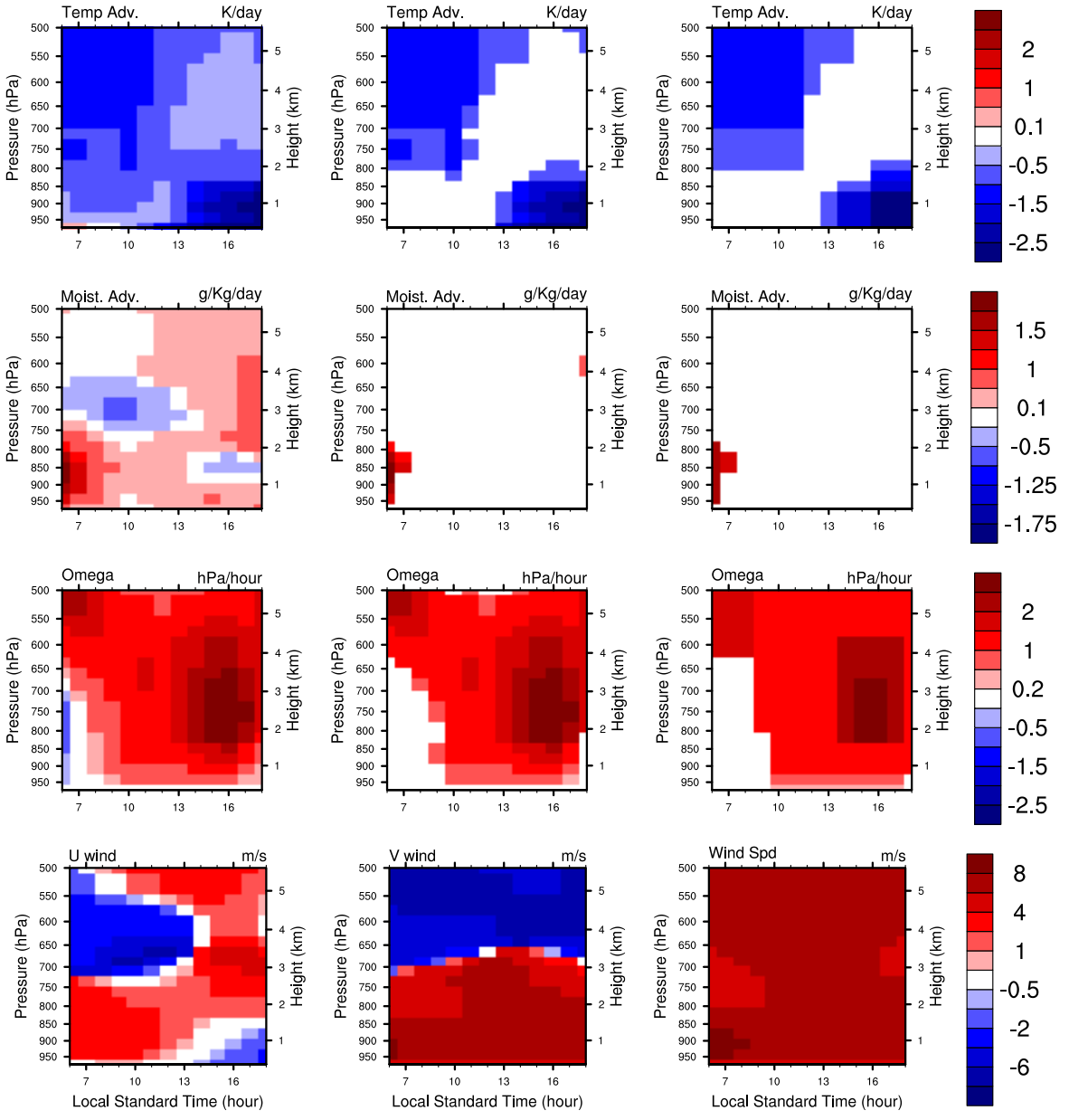

941 FIG. 4. Time-Height composite mean large scale horizontal advective tendency for temperature (top row) and water vapor
942 mixing ratio (second row), subsidence rate (third row) and zonal wind (bottom left), meridional wind (bottom middle) and wind
943 speed (bottom right) for the composite case based on long-term continuous forcing data from variational analysis. In the first three
944 rows, the left figures are the original composite values; the middle figures show the data passing the significance test that values
945 are statistically different from "zero"; and the right figures show our idealization of the forcing.

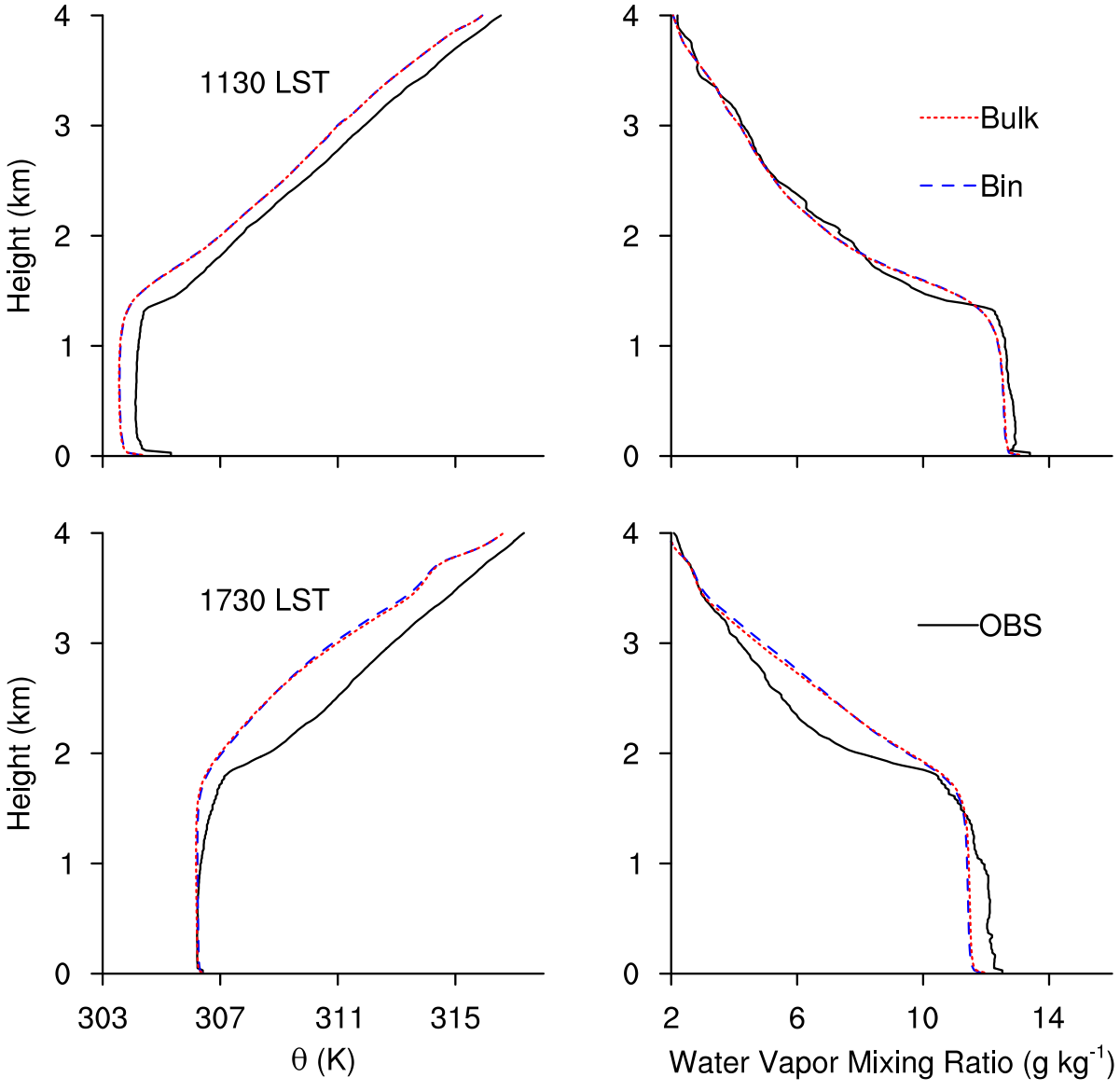

FIG. 5. Vertical profiles of (left) potential temperature and (right) water vapor mixing ratio at (top) 1130 LST and (bottom) 1730 LST.

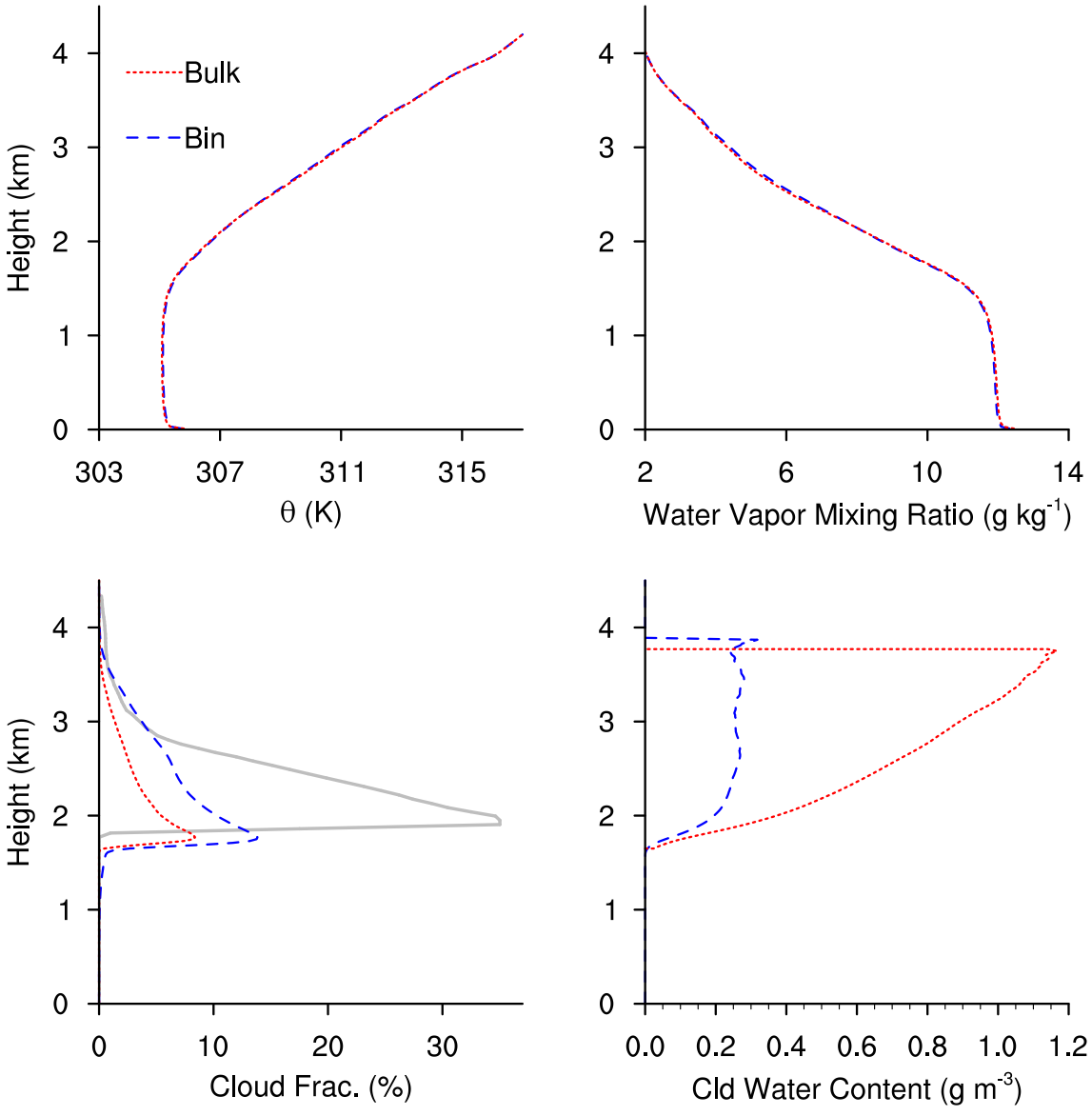

FIG. 6. Vertical profiles of (top left) potential temperature, (top right) water vapor mixing ratio, (bottom left) cloud fraction and (bottom right) in-cloud cloud water content at 1330 LST. Solid grey line denotes observed cloud fraction at 1330 LST.

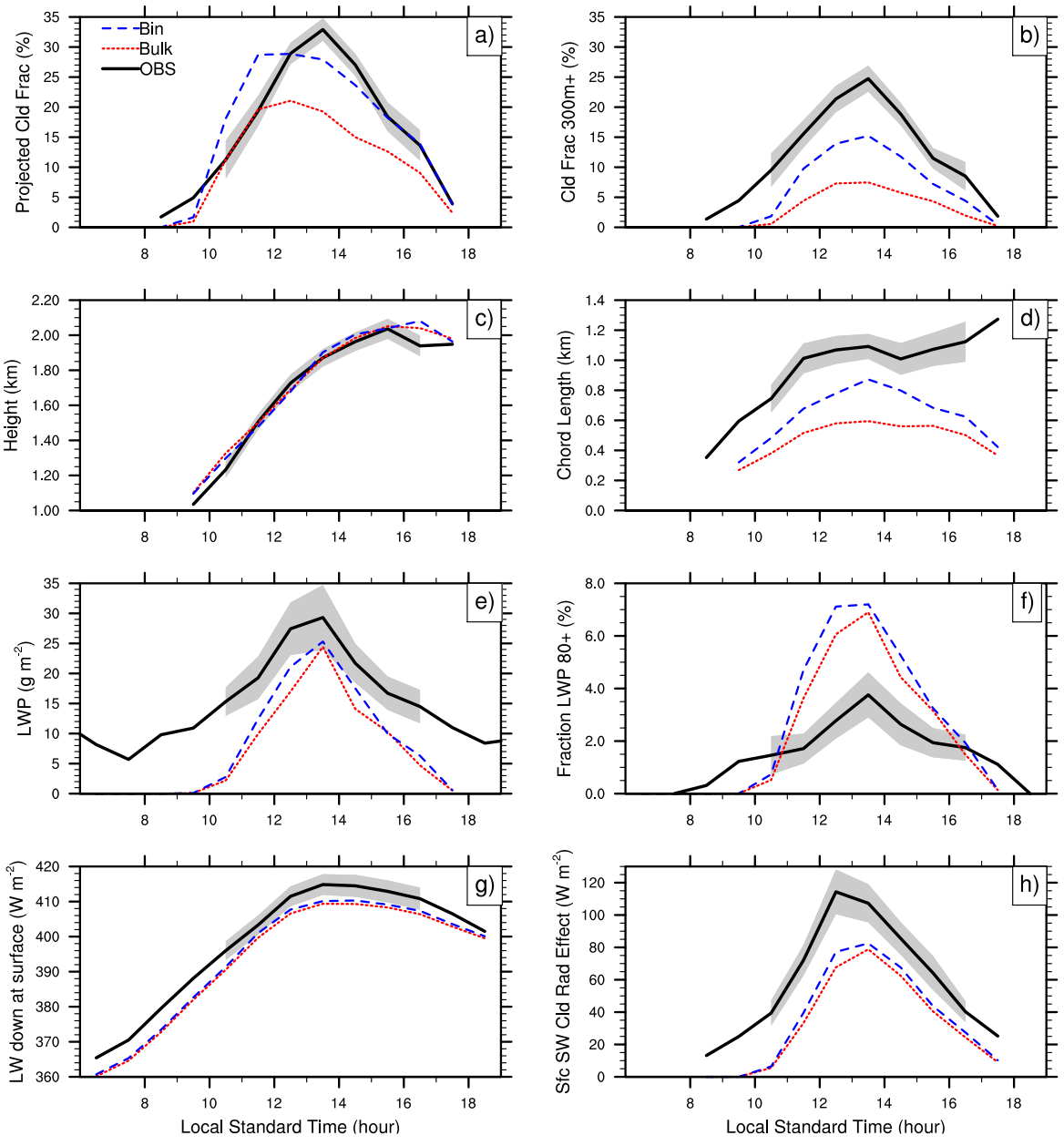

946 FIG. 7. Time series of (a) total projected cloud fraction at the surface, (b) projected cloud fraction with cloud vertical extent
947 greater than 300 meters, (c) average cloud base height and (d) average cloud chord length, (e) liquid water path, (f) projected
948 cloud fraction with liquid water path greater than 80 g m^{-2}, (g) downward longwave radiation at surface and (h) downward cloud
949 shortwave radiative effect at surface from observation (solid black), LES with 1-moment bulk microphysics (bulk, dotted red) and
950 LES with bin spectral microphysics (bin, dashed blue). The width of shading on either side the observed composite mean value
951 denotes one standard error of the mean across all the sample days. The shading is only shown for hours with sample days greater
952 than 30 for the purpose of statistical significance.

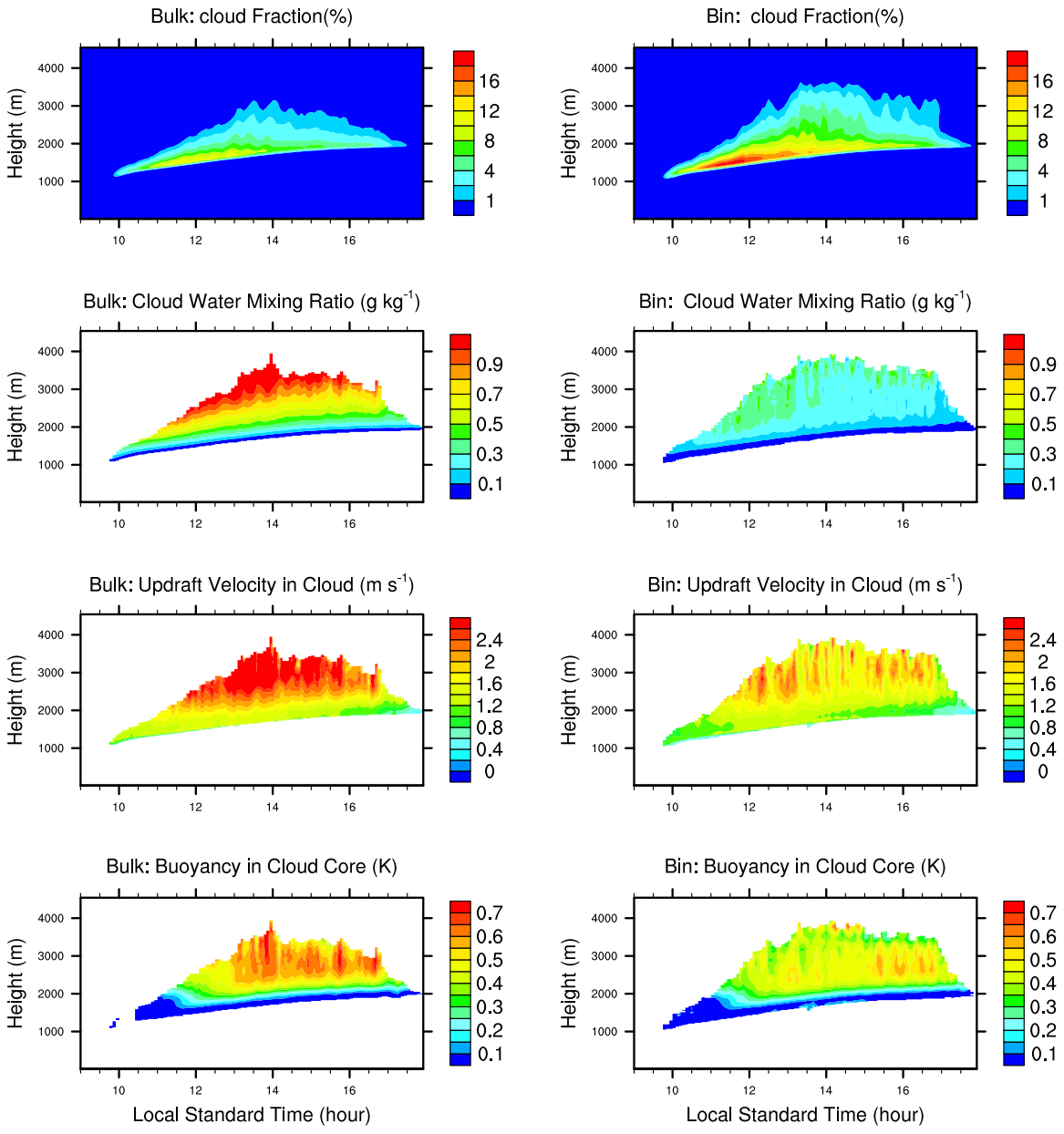

FIG. 8. (Top row) LES cloud fraction with (left) bulk and (right) bin microphysics; (second row) in-cloud total condensate; (third row) in-cloud updraft velocity; (fourth row) buoyancy in the cloud core area.

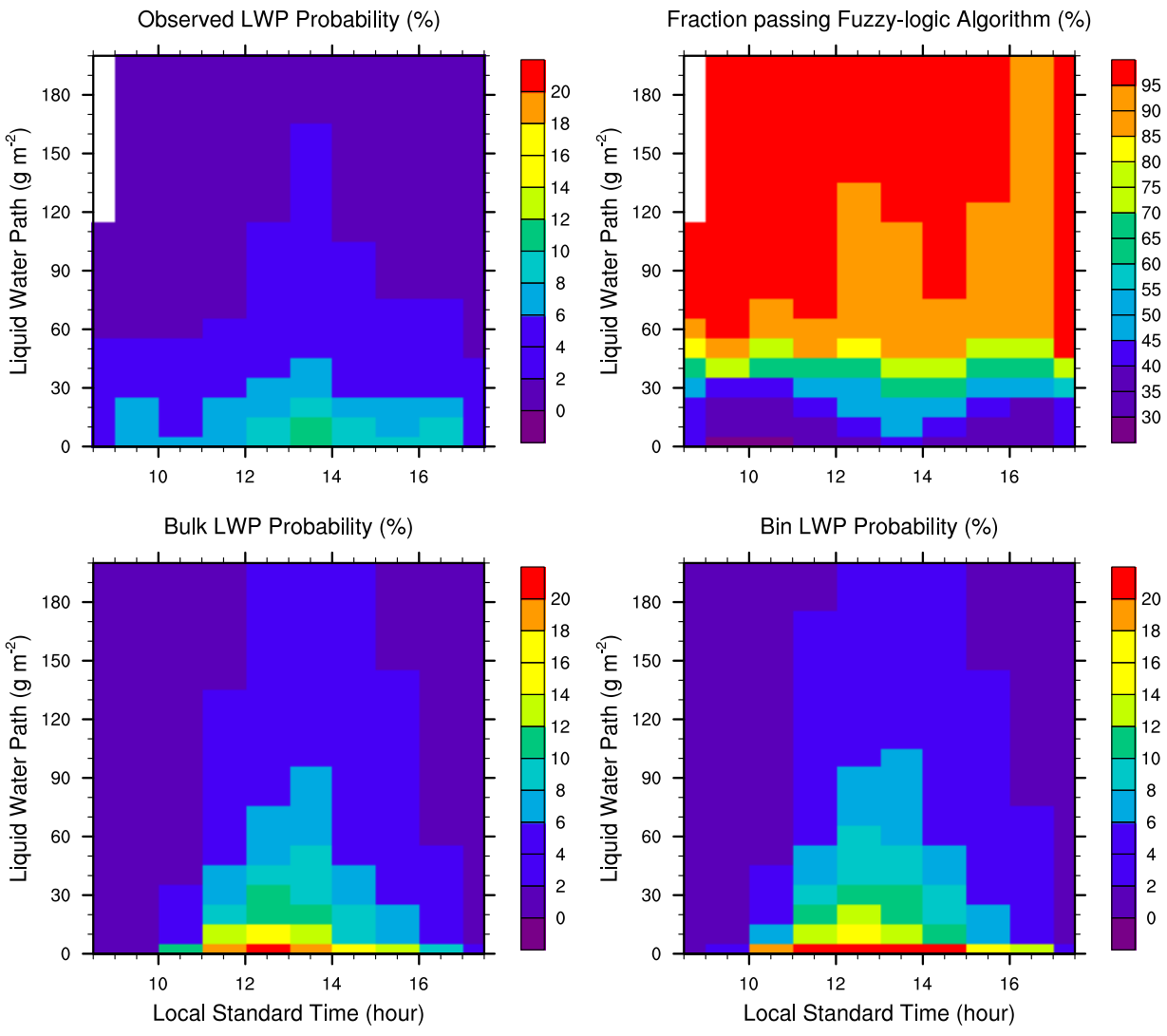

FIG. 9. Observed (top left) liquid water path probability distribution versus local standard time (hour) and (top right) the fraction of occurrence for a radar profile with simultaneous liquid water path observation greater than the reported value to pass the fuzzy logic algorithm for valid vertical velocity retrieval. Bottom rows show the LES liquid water path probability distribution for bulk (bottom left) and bin (bottom right) microphysics runs.

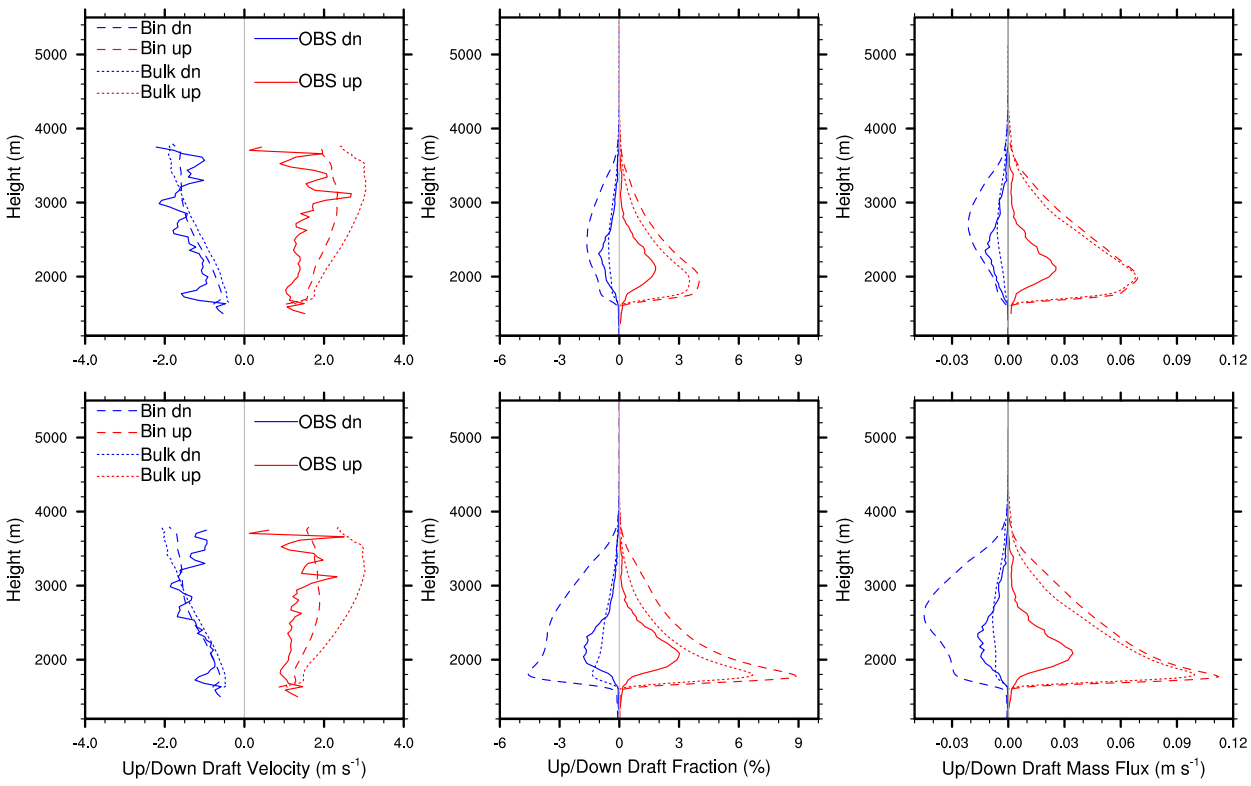

FIG. 10. Comparison at 1330 LST between LES with bin (dashed lines) and bulk (dotted lines) microphysics and radar retrievals (solid lines): (left) vertical velocity for updraft (red) and downdraft (blue); (middle) updraft and downdraft area fractions; (right) updraft and downdraft mass flux. The comparison (top row) is limited to cloudy profiles with liquid water path greater than 80 g m^{-2} in both LES and valid observations. Bottom row is the comparison for all the cloud profiles in LES and all the valid retrievals.

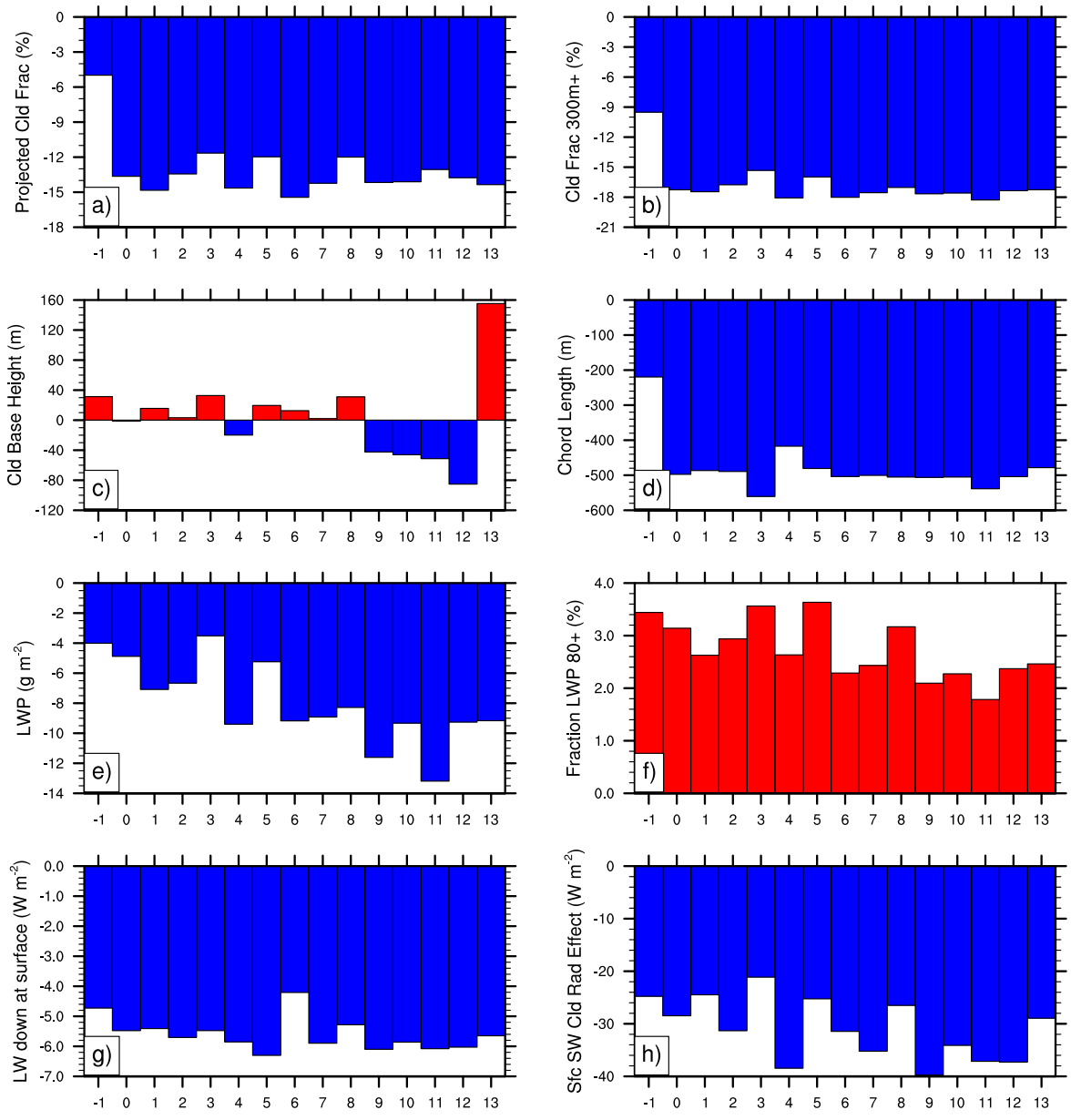

FIG. 11. Model bias (model minus observation) at 1330 LST when shallow cumulus cloud fraction peaks during the day. X-Axis numbers denote the sensitivity tests listed in Table 1.

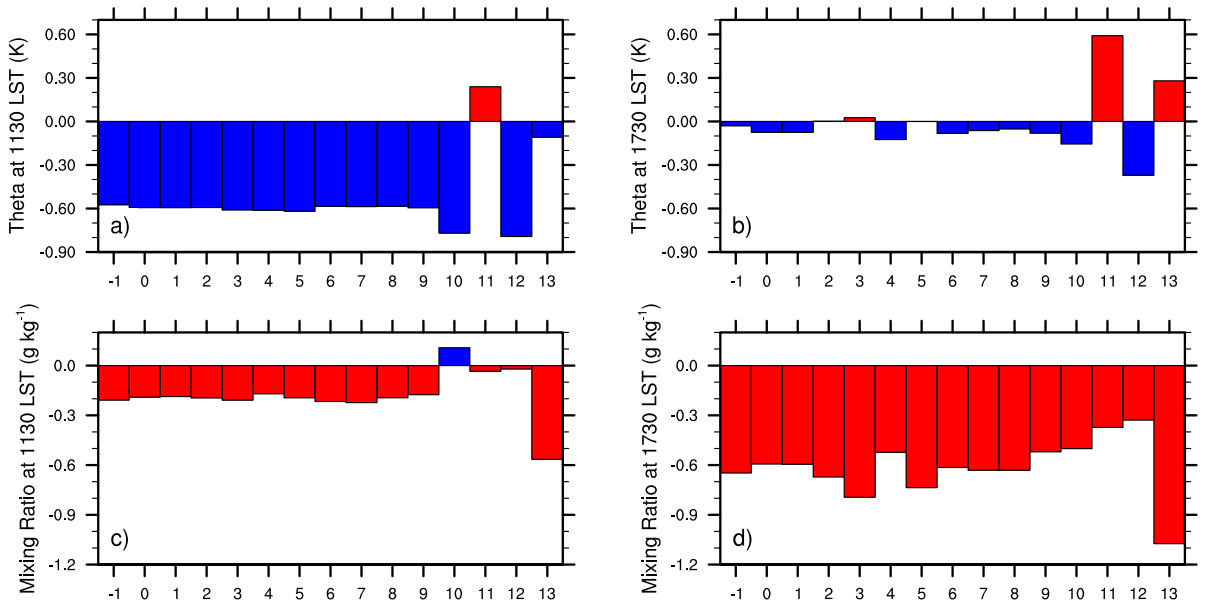

FIG. 12. Model bias (model minus observation) in mixed-layer potential temperature (top) and mixing ratio (bottom) at 1130 LST (left) and 1730 LST (right). X-Axis numbers denote the sensitivity tests listed in Table 1.

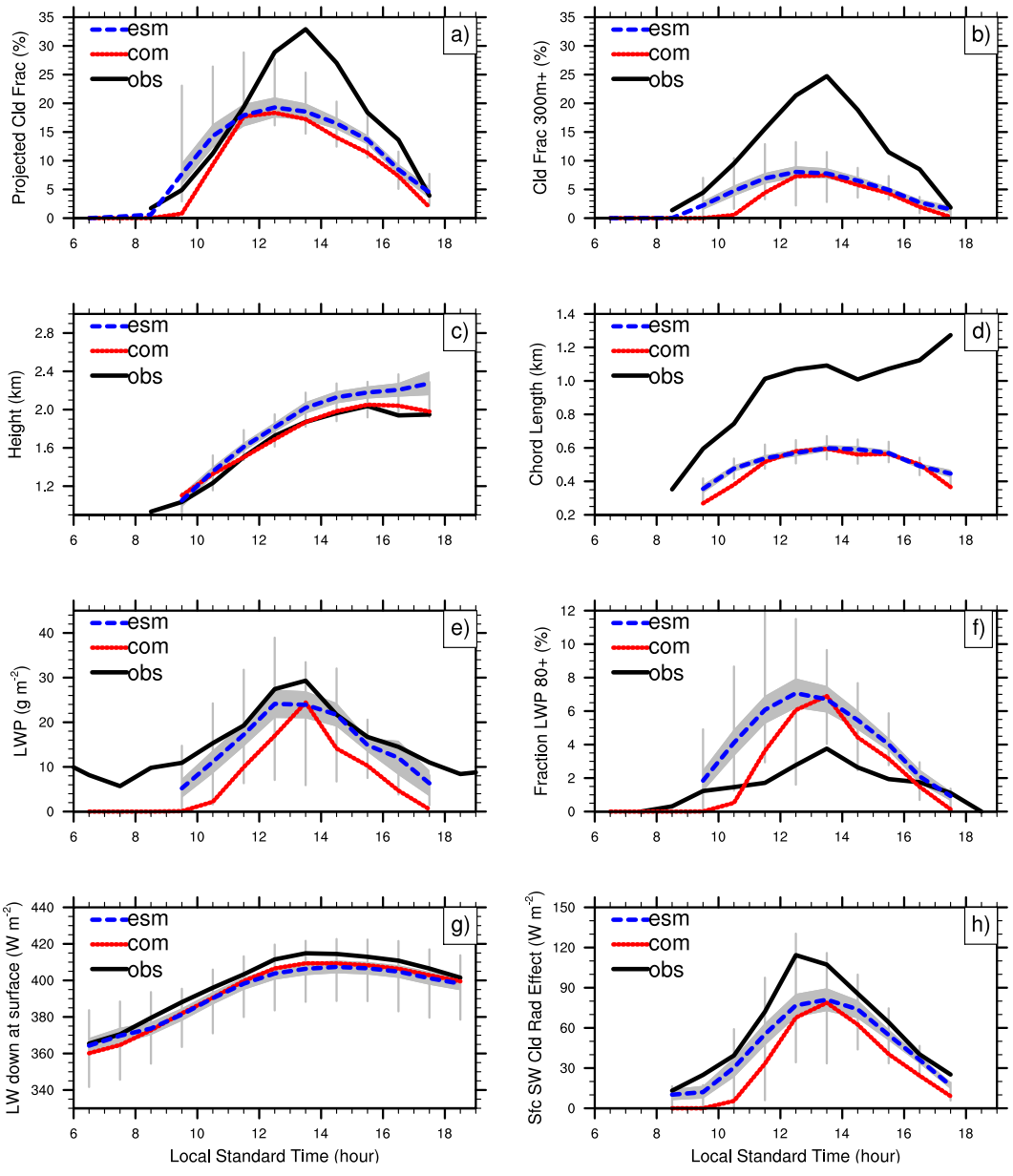

962 FIG. 13. Comparison between observation (black line), ensemble mean of individual day LES runs (blue long dashed line)
963 and the LES of the composite CASS control run (red line). All LES runs are with bulk microphysics. The shaded area around
964 the ensemble mean value denotes the width of one standard error across 40 individual day ensemble runs which produce shallow
965 cumulus clouds. The vertical solid grey lines denote inter-quartile range of the 40 ensemble runs which produce shallow cumulus
966 clouds.